

3D UNWRAPPED PHASE RETRIEVAL WITH CODED APERTURE IS REDUCIBLE TO PROJECTION TOMOGRAPHY

ALBERT FANNJIANG

ABSTRACT. A discrete framework of 3D tomographic phase retrieval with a coded aperture under the Rytov and Born approximations is analyzed. With the introduction of a beam splitter together with coded and uncoded apertures in the measurement, the dataset of diffraction patterns is reducible to that of projections under various measurement uncertainties such as sample heterogeneities, unknown orientations and positions.

Without a beam splitter, this data reducibility holds true for *random conical tilt* (RCT) and *orthogonal tilt* (OT) schemes widely used in cryo-EM if performed with a coded aperture. This approach has the potential of leveraging highly successful projection-based techniques in cryo-EM to process diffraction data collected under uncertainties.

The resulting phase unwrapping problem for 3D projection tomography is solved by the proposed sampling schemes including as special cases (i) the conical tilting of range at least π at a conical angle slightly greater than $\pi/4$, (ii) the orthogonal dual-axis tilting of a tilt range at least $\pi/2$ for each axis and (iii) a combination of a conical tilting of range at least $\pi/2$ at any conical angle $\tau \in (\pi/4, \pi/2]$ and an orthogonal single-axis tilting of a tilt range at least τ .

1. INTRODUCTION

Diffraction plays a central role in *ab initio* structure determination by high resolution X-ray and electron microscopies due to high sensitivity of phase contrast mechanism [2, 26, 32]. Compared to the real-space imaging with lenses such as transmission electron microscopy, lensless diffraction methods are aberration free and have the potential for delivering equivalent resolution with fewer photons/electrons [14, 34].

While single crystal X-ray diffraction remains as the most widely used technique for structural determination, a complete diffraction data set with a signal-to-noise ratio (SNR) of 2 at 2Å resolution requires at a minimum crystal size of 1.8 micron in theory [33]. However, limited crystallinity of many materials often makes it challenging to obtain sufficiently large and well-ordered crystals for X-ray diffraction. In addition, the so called crystallographic phase problem arises with macroscopic crystals as a result of fundamental under-sampling of diffraction patterns highly concentrated at the Bragg peaks [44].

On the other hand, extremely intense X-ray free-electron lasers (XFELs) have driven the development of serial crystallography with sub-micron sized crystals, a technique that is also increasingly applied at synchrotron sources as well [6, 8]. Here acquiring snapshots from many tiny crystals instead of a rotation series from a single crystal avoids dose accumulation, henceforth permitting higher fluence and smaller diffracting volume, without the need for cryogenic cooling. Despite of the high intensity of XFEL pulses, the short femtosecond pulse duration can outrun radiation damage effects in so called *serial femtosecond nanocrystallography* (SFX). This process of “diffraction-before-destruction” allows the

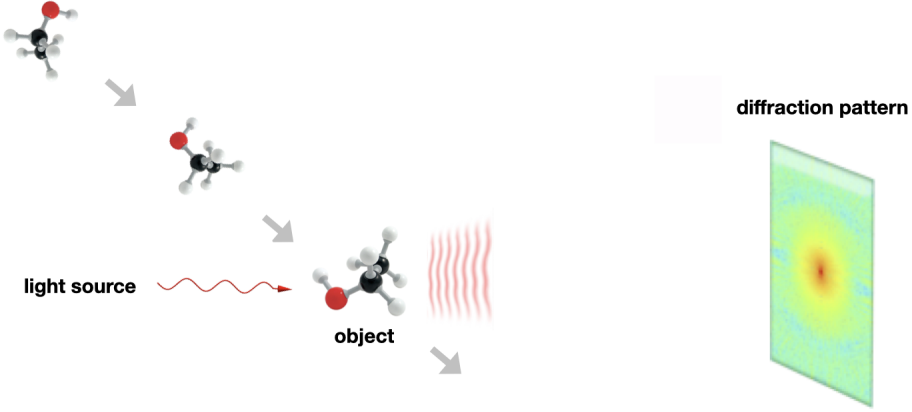


FIGURE 1. Serial crystallography: A stream of identical particles of various orientations scatter incident X-ray with diffraction patterns measured at far field.

pristine radiation-damage-free state of the object to be recorded with the unique benefit of pulse-intensity-limited, instead of radiation-damage limited, SNR [37, 48].

Despite the electron's $10^4 - 10^6$ times stronger scattering cross section than X-ray's, the diffraction-before-destruction regime requires the coherent concentration of about 10^7 electrons to femtosecond duration, a still challenging feat due to pulse broadening effects such as Coulomb repulsion and energy dispersion [3, 62]. As a result, electron diffraction/microscopy for structural determination is currently performed with low dose and cryo-cooling to mitigate radiation damage.

All of the above methods attempt lens-less 3D structural determination from the diffraction patterns of identical particles of various orientations, which collectively will be referred to in this paper as *3D phase retrieval* (see Figure 1 and 2).

In contrast to 3D phase retrieval, single-particle cryo-electron microscopy (cryo-EM) produces, through electromagnetic lenses, real-space images of many well-separated sub-micron sized particles. These images are object projections convoluted by a point-spread function, due to lens aberration and aperture limitation, and contain both amplitude and phase information. Hence there is no "phase problem" as in X-ray crystallography [24]. But in comparison to lensless electron diffraction, cryo-EM's lens-based advantage comes at a substantial cost in SNR [14, 26].

Likewise, conventional X-ray computed tomography (CT), while ignoring diffraction effect, uses absorption as the dominant contrast mechanism and produces real space images that are object projections (via Beer-Lambert's law) convoluted with a point spread function representing the measurement device [46]. The difference is that X-ray CT usually deals with macroscopic objects with full control of orientation while in cryo-EM, single particles' orientations are random and need to be sorted out from electron micrographs. While single particles entail random orientations for both cryo-EM and SFX, the former is more mature in detector technology [23], sample preparation as well as software development. Cryo-EM has the capacity of atomic resolution and is currently the dominant method of choice when the samples are macromolecules of limited crystallinity [5, 13, 26].

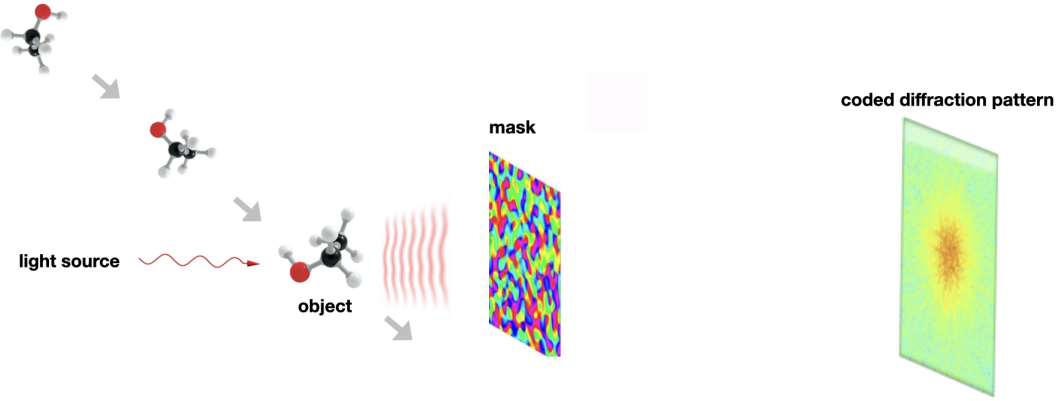


FIGURE 2. Serial crystallography with a coded aperture

For lack of a better term, we shall refer to 3D structural determination from projection data (or their nonlinear functions, c.f. (6)), with the delta function as the point-spread function, as *pure projection tomography* or simply *projection tomography* (PT). In other words, PT is the idealized set-up of cryo-EM and X-ray CT. Depending on the context we shall refer to either a (coded or uncoded) diffraction pattern or a projection as a “snapshot”.

The basic thesis of the present work is that under noiseless measurements with a coded aperture (Figure 2), 3D phase retrieval is informationally equivalent to PT under various proposed measurement schemes. Our motivation is that a projection data set is much better suited for particle classification and orientation alignment. Instead of performing classification and alignment with diffraction patterns, as usually practiced [35, 41, 56], it should be a better strategy to first transform a diffraction data set into a projection data set (at least when SNR is greater than 1. See Section 10 for discussion about the noise issue at SNR much less than 1.) and then leverage the advanced techniques of classifying and aligning projection data, a main driving force behind the successes of single-particle cryo-EM [42, 53, 55].

A key piece of our approach is the introduction of a beam splitter which directs the beams through a coded and uncoded aperture and thus provides two independent snapshots of the same exit waves (Figure 3). The combination of a coded and uncoded aperture enables the reduction of diffraction pattern data to projection data (Section 6 and 7). Importantly, the reduction process does not rely on the knowledge of the relative position and orientation between the object frame and the device frame and is immune to various measurement uncertainties discussed in more details in Section 5.

We extend the analysis to the widely used schemes of random conical tilt and orthogonal tilt from cryo-EM [24, 39], both of which collect *pairwise* measurement data by rotating the sample holder. Instead of the beam splitter, the relative orientation information provided by different sample tilts facilitates data reducibility for these schemes if carried out with a coded aperture (Section 8).

In Section 9, we present phase unwrapping schemes for the resulting 3D projection tomography including three readily implementable examples: (i) A conical tilting of range at least π at a conical angle slightly greater than $\pi/4$; (ii) An orthogonal dual-axis tilting of a tilt range at least $\pi/2$ for each axis; (iii) A combination of a conical tilting of range at least $\pi/2$

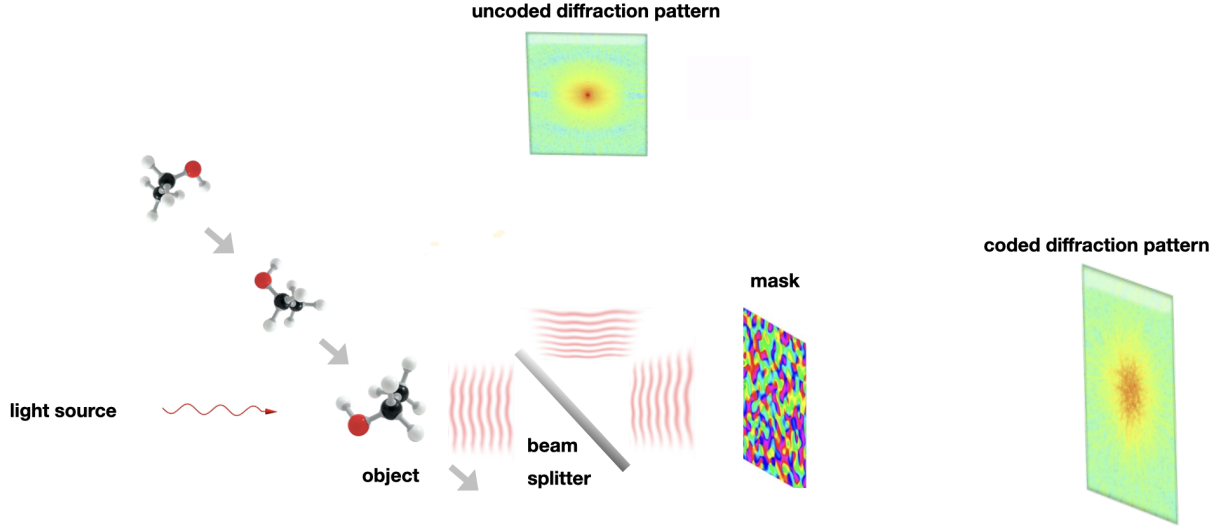


FIGURE 3. Simultaneous measurement of two diffraction patterns, one coded and one uncoded, with a beam splitter.

at any conical angle $\tau \in (\pi/4, \pi/2]$ and an orthogonal single-axis tilting of a tilt range at least τ . It turns out that the widely used single-axis tilting can not unambiguously unwrap the phases in general regardless of the tilt range.

In the rest of the paper, we first discuss the continuous forward model in Section 2, a discrete framework in Section 3 and coded diffraction patterns in Section 4. We conclude in Section 10 with a discussion on the noise issue.

2. FORWARD MODEL

Let us review the forward model of 3D phase retrieval with a coded aperture.

In 3D diffractive imaging, the thickness of the object is no longer negligible and the X-ray propagation through the object must be accurately modeled. This is often accomplished by an approximate solution to the Helmholtz equation

$$(1) \quad \Delta u(\mathbf{r}) + \kappa^2 n^2(\mathbf{r})u(\mathbf{r}) = 0, \quad \mathbf{r} = (x, y, z)$$

where $\kappa = 2\pi/\lambda$ is the wavenumber and $n(\mathbf{r}) \in \mathbb{C}$ is the complex refractive index of the object. The real and imaginary components of n describe the dispersive and absorptive aspects of the wave-matter interaction. The real part of n is directly related to electron density in the case of X-ray and Coulomb field in the case of electron waves.

In X-ray [64] as well as high-energy electron [31], the object is approximately modeled as a quasi-phase object with the far field

$$(2) \quad u(\mathbf{r}) = u_i(\mathbf{r})e^{i\kappa\psi(\mathbf{r})},$$

the incident wave $u_i = e^{i\kappa z}$ and the surrogate function ψ

$$(3) \quad \psi(x, y) = \frac{1}{2} \int (n^2(x, y, z) - 1) dz = \int f(x, y, z) dz, \quad f := (n^2 - 1)/2.$$

The integral in (3) is the *z-projection* of the object f .

In electron diffraction, (2)-(3) is known as the high-energy approximation [31] while in optics, it is known as the Rytov approximation in the high frequency limit [46, 52]. It resembles the geometrical optics and hence describes some features of multiple (small-angle) scattering. On the other hand, unlike geometrical optics, the Rytov approximation also includes diffraction effect and allows large phase fluctuations for many applications, representing a significant improvement over the Born approximation (a.k.a. the *weak-phase-object approximation* in cryo-EM [24]) which amounts to

$$(4) \quad e^{i\kappa\psi} \approx 1 + i\kappa\psi$$

for $\kappa|\psi| \ll 1$.

However, the phase fluctuations appearing in the exponent implies that u yields only the information of the projection ψ modulo $4\pi/\kappa$, hence the problem of *phase unwrapping* [10, 29]. The solution for phase unwrapping is critical in revealing the depth dimension of the object. Phase unwrapping problem does not present in X-ray CT, which neglects diffraction, or cryo-EM, which operates under the Born approximation.

For the set-up of Figure 2, after the X-ray exits the object, the exit wave is then masked by a random mask μ with the far field at the detector given by

$$(5) \quad \mathcal{F}[u_i e^{i\kappa\psi} \odot \mu]$$

where \mathcal{F} is the Fourier transform. The detector, however, measures only the intensities of the far field, erasing the phase information.

In contrast, the PT's data set under the Rytov approximation consists of the complex exponential of projections:

$$(6) \quad u_i e^{i\kappa\psi}$$

where ψ is an object projection in the direction of optical axis.

We will analyze measurement schemes that are combinations of coded and uncoded apertures under the Rytov and Born approximations. But first we have to discuss a framework for discretizing the forward model.

3. DISCRETE SET-UP

To describe tomographic experiments, we need two reference frames: the object frame xyz attached to the object and the device frame XYZ with Z as the optical axis ($z = Z$ in Section 2).

Following the framework in [1] we first discretize the object with respect to the object frame. The goal is to establish the discrete version of the Fourier slice theorem (Proposition 3.1).

Let $\llbracket k, l \rrbracket$ denote the integers between and including the integers k and l . We define a 3D $n \times n \times n$ object as the set

$$(7) \quad f = \{f(i, j, k) \in \mathbb{C} : i, j, k \in \mathbb{Z}_n\}$$

where

$$(8) \quad \mathbb{Z}_n = \begin{cases} \llbracket -n/2, n/2 - 1 \rrbracket & \text{if } n \text{ is an even integer;} \\ \llbracket -(n-1)/2, (n-1)/2 \rrbracket & \text{if } n \text{ is an odd integer.} \end{cases}$$

We define three families of line segments, the x -lines, y -lines, and z -lines. Formally, a x -line, denoted by $\ell_{x(\alpha,\beta)}(c_1, c_2)$, is defined as

$$(9) \quad \ell_{x(\alpha,\beta)}(c_1, c_2) : \begin{bmatrix} y \\ z \end{bmatrix} = \begin{bmatrix} \alpha x + c_1 \\ \beta x + c_2 \end{bmatrix} \quad c_1, c_2 \in \mathbb{Z}_{2n-1}, \quad x \in \mathbb{Z}_n$$

To avoid wraparound of x -lines with $|\alpha|, |\beta| \leq 1$, we can zero-pad f in a larger lattice \mathbb{Z}_p^3 with $p \geq 2n-1$. This is particularly important when it comes to define the X-ray transform by a line sum (cf. (16)-(18)) without wrapping around the object domain.

Similarly, a y -line and a z -line are defined as

$$(10) \quad \ell_{y(\alpha,\beta)}(c_1, c_2) : \begin{bmatrix} x \\ z \end{bmatrix} = \begin{bmatrix} \alpha y + c_1 \\ \beta y + c_2 \end{bmatrix} \quad c_1, c_2 \in \mathbb{Z}_{2n-1}, \quad y \in \mathbb{Z}_n,$$

$$(11) \quad \ell_{z(\alpha,\beta)}(c_1, c_2) : \begin{bmatrix} x \\ y \end{bmatrix} = \begin{bmatrix} \alpha z + c_1 \\ \beta z + c_2 \end{bmatrix} \quad c_1, c_2 \in \mathbb{Z}_{2n-1}, \quad z \in \mathbb{Z}_n.$$

We denote the sets of all x -lines, y -lines, and z -lines by \mathcal{L}_x , \mathcal{L}_y , and \mathcal{L}_z , respectively.

Also, we denote the family of lines that corresponds to a fixed pair (α, β) and variable intercepts (c_1, c_2) by $\ell_{x(\alpha,\beta)}$, $\ell_{y(\alpha,\beta)}$ and $\ell_{z(\alpha,\beta)}$ for a family of parallel x -lines, y -lines, and z -lines, respectively. Note that $\ell_{x(1,\beta)} = \ell_{y(1,\beta)}$, $\ell_{x(\alpha,1)} = \ell_{z(1,\alpha)}$ and $\ell_{y(\alpha,1)} = \ell_{z(\alpha,1)}$.

Let f_x be the continuous interpolation of f in the directions perpendicular to x as follows:

$$(12) \quad f_x(i, y, z) = \sum_{j \in \mathbb{Z}_n} \sum_{k \in \mathbb{Z}_n} f(i, j, k) D_p(y - j) D_p(z - k), \quad y, z \in \mathbb{R}$$

where D_p is the p -periodic Dirichlet kernel given by

$$(13) \quad D_p(t) = \frac{1}{p} \sum_{l \in \mathbb{Z}_p} e^{i 2\pi l t / p} = \begin{cases} 1, & t = mp, \quad m \in \mathbb{Z} \\ \frac{\sin(\pi t)}{p \sin(\pi t/p)}, & \text{else.} \end{cases}$$

In particular, $[D_p(i - j)]_{i,j \in \mathbb{Z}_p}$ is the $p \times p$ identity matrix.

Similarly we define the interpolation of f perpendicular to y and z , respectively, as

$$(14) \quad f_y(x, j, z) = \sum_{i \in \mathbb{Z}_n} \sum_{k \in \mathbb{Z}_n} f(i, j, k) D_p^2(x - i, z - k), \quad x, z \in \mathbb{R};$$

$$(15) \quad f_z(x, y, k) = \sum_{i \in \mathbb{Z}_n} \sum_{j \in \mathbb{Z}_n} f(i, j, k) D_p^2(x - i, y - j), \quad x, y \in \mathbb{R},$$

where

$$D_p^2(\mathbf{k}) := D_p(k_1) D_p(k_2), \quad \mathbf{k} = (k_1, k_2)$$

is the 2D p -periodic Dirichlet kernel.

By interpolating from the grid points (12)-(15), we have extended f from \mathbb{Z}_p^3 to the hyperplanes $x = i$, $y = j$ or $z = k$, where $i, j, k \in \mathbb{Z}_p$.

Having extended the domain of f to the hyperplanes $x = i$, $y = j$ or $z = k$, where $i, j, k \in \mathbb{Z}_{2n-1}$, we define the discrete projections as the following line sums

$$(16) \quad f_{x(\alpha,\beta)}(c_1, c_2) = \sum_{i \in \mathbb{Z}_n} f_x(i, \alpha i + c_1, \beta i + c_2),$$

$$(17) \quad f_{y(\alpha,\beta)}(c_1, c_2) = \sum_{j \in \mathbb{Z}_n} f_y(\alpha j + c_1, j, \beta j + c_2)$$

$$(18) \quad f_{z(\alpha,\beta)}(c_1, c_2) = \sum_{k \in \mathbb{Z}_n} f_z(\alpha k + c_1, \beta k + c_2, k)$$

with $c_1, c_2 \in \mathbb{Z}_{2n-1}$. With zero-padding, we define projections on \mathbb{Z}_p^2 , for $p \geq 2n - 1$.

The 3D Fourier transform \hat{f} of the object f , supported in \mathbb{Z}_n^3 , is given by

$$(19) \quad \hat{f}(\xi, \eta, \zeta) = \sum_{i,j,k \in \mathbb{Z}_n} f(i, j, k) e^{-i2\pi(\xi i + \eta j + \zeta k)/p} = \sum_{i,j,k \in \mathbb{Z}_p} f(i, j, k) e^{-i2\pi(\xi i + \eta j + \zeta k)/p}$$

where the range of the Fourier variables ξ, η, ζ can be extended from the discrete interval \mathbb{Z}_p to the continuum $[-(p-1)/2, (p-1)/2]$. Note that by definition, \hat{f} is a p -periodic band-limited function. The associated 1-D and 2-D (partial) Fourier transforms are similarly defined p -periodic band-limited functions.

3.1. Projection support constraint. The actual support of the projections (16)-(18) for $0 \leq \alpha, \beta \leq 1$ and odd integer n , for example, is contained in

$$(20) \quad \bigcup_{i \in \mathbb{Z}_n} (\mathbb{Z}_n - \lfloor \alpha i \rfloor) \times (\mathbb{Z}_n - \lfloor \beta i \rfloor)$$

where $\lfloor \cdot \rfloor$ denotes the floor function. In turn, the set in (20) is a subset of

$$(21) \quad \left\{ \bigcup_{i \in \mathbb{Z}_n} (\mathbb{Z}_n - \lfloor \alpha i \rfloor) \right\} \times \left\{ \bigcup_{i \in \mathbb{Z}_n} (\mathbb{Z}_n - \lfloor \beta i \rfloor) \right\} = \mathbb{Z}_{\ell_\alpha} \times \mathbb{Z}_{\ell_\beta}$$

where

$$(22) \quad \ell_\alpha = 2 \cdot \lfloor \frac{1}{2}(1 + |\alpha|)(n-1) \rfloor + 1, \quad \ell_\beta = 2 \cdot \lfloor \frac{1}{2}(1 + |\beta|)(n-1) \rfloor + 1.$$

The same support constraint $\mathbb{Z}_{\ell_\alpha} \times \mathbb{Z}_{\ell_\beta}$ with (22) applies to the case with $|\alpha|, |\beta| \leq 1$ and odd integer n .

3.2. Fourier slices and common lines. The Fourier slice theorem concerns the 2-D discrete Fourier transform $\hat{f}_{x(\alpha,\beta)}$ defined as

$$(23) \quad \hat{f}_{x(\alpha,\beta)}(\eta, \zeta) = \sum_{j,k \in \mathbb{Z}_n} f_{x(\alpha,\beta)}(j, k) e^{-i2\pi(\eta j + \zeta k)/p},$$

and the 3-D discrete Fourier transform given in (19) where the ξ, η and ζ are the coordinates of the Fourier space in the object frame.

It is straightforward, albeit somewhat tedious, to derive the discrete Fourier slice theorem which plays an important role in our analysis.

Proposition 3.1. [1] (Fourier slice theorem) For a given family of x -lines $\ell_x(\alpha, \beta)$ with fixed slopes (α, β) and variable intercepts (c_1, c_2) . Then the 2D discrete Fourier transform $\widehat{f}_{x(\alpha, \beta)}$ of the x -projection $f_{x(\alpha, \beta)}$ and the 3D discrete Fourier transform \widehat{f} of the object f satisfy the equation

$$(24) \quad \widehat{f}_{x(\alpha, \beta)}(\eta, \zeta) = \widehat{f}(-\alpha\eta - \beta\zeta, \eta, \zeta).$$

Likewise, we have

$$(25) \quad \widehat{f}_{y(\alpha, \beta)}(\xi, \zeta) = \widehat{f}(\xi, -\alpha\xi - \beta\zeta, \zeta),$$

$$(26) \quad \widehat{f}_{z(\alpha, \beta)}(\xi, \eta) = \widehat{f}(\xi, \eta, -\alpha\xi - \beta\eta).$$

For ease of notation, we denote by \mathbf{t} the direction of projection, $x(\alpha, \beta)$, $y(\alpha, \beta)$ or $z(\alpha, \beta)$ in the reference frame attached to the object. Let $P_{\mathbf{t}}$ denote the origin-containing (continuous) plane orthogonal to \mathbf{t} in the Fourier space and let $L_{\mathbf{t}_1, \mathbf{t}_2} := P_{\mathbf{t}_1} \cap P_{\mathbf{t}_2}$ be the common line for $\mathbf{t}_1, \mathbf{t}_2$ not parallel to each other. A corollary then is that $L_{\mathbf{t}_1, \mathbf{t}_2}$ is the 1-D Fourier transform of the iterated projections (in $\mathbf{t}_1, \mathbf{t}_2$) of the 3D object.

Finally, we note the covariance property w.r.t. spatial shift of the discrete projection as follows.

Instead of the definition (16), define the discrete projection with additional offsets d_1, d_2 as

$$(27) \quad f'_{x(\alpha, \beta)}(c_1, c_2) = \sum_{i \in \mathbb{Z}_n} f_x(i, \alpha i + c_1 + d_1, \beta i + c_2 + d_2).$$

By the same derivation of Proposition 3.1, we have

$$(28) \quad \begin{aligned} \widehat{f}'_{x(\alpha, \beta)}(\eta, \zeta) &= \widehat{f}(-\alpha\eta - \beta\zeta, \eta, \zeta) e^{i2\pi(\eta d_1 + \zeta d_2)/p} \\ &= \widehat{f}_{x(\alpha, \beta)}(\eta, \zeta) e^{i2\pi(\eta d_1 + \zeta d_2)/p} \end{aligned}$$

which amounts to, unsurprisingly, a spatial shift of the projection $f_{x(\alpha, \beta)}$, i.e.

$$f'_{x(\alpha, \beta)}(c_1, c_2) = f_{x(\alpha, \beta)}(c_1 - d_1, c_2 - d_2).$$

Thus by (28), the uncoded diffraction pattern has the invariance property

$$(29) \quad |\widehat{f}'_{x(\alpha, \beta)}|^2(\eta, \zeta) = |\widehat{f}_{x(\alpha, \beta)}|^2(\eta, \zeta).$$

4. DIFFRACTION PATTERN

Let \mathcal{T} denote the set of directions \mathbf{t} employed in the tomographic measurement, which can be coded (as in Figure 2) or uncoded (as in Figure 1). To fix the idea, let $p = 2n - 1$ in (13).

Let the Fourier transform \mathcal{F} of the projection $e^{i\kappa f_{\mathbf{t}}(\mathbf{n})}$ be written as

$$F_{\mathbf{t}}(e^{-i2\pi\mathbf{w}}) = \sum_{\mathbf{n} \in \mathbb{Z}_p^2} e^{-i2\pi\mathbf{n} \cdot \mathbf{w}} e^{i\kappa f_{\mathbf{t}}(\mathbf{n})}, \quad \mathbf{w} \in \left[-\frac{1}{2}, \frac{1}{2} \right]^2.$$

In the absence of a random mask ($\mu \equiv 1$), the intensities of the Fourier transform can be written as

$$(30) \quad |F_{\mathbf{t}}(e^{-i2\pi\mathbf{w}})|^2 = \sum_{\mathbf{n} \in \mathbb{Z}_{2p-1}^2} \left\{ \sum_{\mathbf{n}' \in \mathbb{Z}_p^2} e^{i\kappa f_{\mathbf{t}}(\mathbf{n}' + \mathbf{n})} e^{-i\kappa \overline{f_{\mathbf{t}}(\mathbf{n}')}} \right\} e^{-i2\pi \mathbf{n} \cdot \mathbf{w}}, \quad \mathbf{w} \in \left[-\frac{1}{2}, \frac{1}{2} \right]^2,$$

which is called the uncoded diffraction pattern in the direction \mathbf{t} . Here and below the over-line notation means complex conjugacy. The expression in the brackets in (30) is the autocorrelation function of $e^{i\kappa f_{\mathbf{t}}}$.

The diffraction patterns are then uniquely determined by sampling on the grid

$$(31) \quad \mathbf{w} \in \frac{1}{2p-1} \mathbb{Z}_{2p-1}^2$$

or by Kadec's 1/4-theorem on any following irregular grid [65]

$$(32) \quad \{\mathbf{w}_{jk}, \ j, k \in \mathbb{Z}_{2p-1} : |(2p-1)\mathbf{w}_{jk} - (j, k)| < 1/4\}.$$

With the Nyquist, regular (31) or irregular (32), sampling, the diffraction pattern contains the same information as does the autocorrelation function of $f_{\mathbf{t}}$.

The following result is our basic tool.

Proposition 4.1. [17] *Let μ be the phase mask with phase continuously and independently distributed. If $e^{i\kappa g_{\mathbf{t}}} \odot \nu$ produces the same diffraction pattern as $e^{i\kappa f_{\mathbf{t}}} \odot \mu$, then for some $\mathbf{m}_{\mathbf{t}} \in \mathbb{Z}^2, \theta_{\mathbf{t}} \in \mathbb{R}$*

$$(33) \quad e^{i\kappa g_{\mathbf{t}}(\mathbf{n})} \nu(\mathbf{n}) = \begin{cases} e^{i\theta_{\mathbf{t}}} e^{i\kappa f_{\mathbf{t}}(\mathbf{n} + \mathbf{m}_{\mathbf{t}})} \mu(\mathbf{n} + \mathbf{m}_{\mathbf{t}}) \\ e^{i\theta_{\mathbf{t}}} e^{-i\kappa \overline{f_{\mathbf{t}}(-\mathbf{n} + \mathbf{m}_{\mathbf{t}})}} \overline{\mu(-\mathbf{n} + \mathbf{m}_{\mathbf{t}})}. \end{cases}$$

for all \mathbf{n} .

After taking logarithm, (33) becomes

$$(34) \quad \kappa g_{\mathbf{t}}(\mathbf{n}) - i \ln \nu(\mathbf{n}) = \begin{cases} \theta_{\mathbf{t}} + \kappa f_{\mathbf{t}}(\mathbf{n} + \mathbf{m}_{\mathbf{t}}) - i \ln \mu(\mathbf{n} + \mathbf{m}_{\mathbf{t}}) \\ \theta_{\mathbf{t}} - \kappa \overline{f_{\mathbf{t}}(-\mathbf{n} + \mathbf{m}_{\mathbf{t}})} - i \ln \overline{\mu(-\mathbf{n} + \mathbf{m}_{\mathbf{t}})} \end{cases} \mod 2\pi.$$

If μ is completely known, i.e. $\nu = \mu$, then (34) becomes

$$(35) \quad \kappa g_{\mathbf{t}}(\mathbf{n}) - i \ln \mu(\mathbf{n}) = \begin{cases} \theta_{\mathbf{t}} + \kappa f_{\mathbf{t}}(\mathbf{n} + \mathbf{m}_{\mathbf{t}}) - i \ln \mu(\mathbf{n} + \mathbf{m}_{\mathbf{t}}) \\ \theta_{\mathbf{t}} - \kappa \overline{f_{\mathbf{t}}(-\mathbf{n} + \mathbf{m}_{\mathbf{t}})} - i \ln \overline{\mu(-\mathbf{n} + \mathbf{m}_{\mathbf{t}})} \end{cases} \mod 2\pi.$$

Our goal is to prove that with a sufficiently large \mathcal{T} , (35) yields $g = f$ and $\mu = \nu$, up to a constant phase factor, almost surely, i.e. $\mathbf{m}_{\mathbf{t}} = 0$ and $\theta_{\mathbf{t}} = \text{const.}$ for all \mathbf{t} .

5. INFORMATION EQUIVALENCE UNDER UNCERTAINTIES

In conventional X-ray crystallography, a single millimeter-sized crystal's position and orientation can be precisely adjusted by a goniometer to produce a complete set of diffraction patterns [33]. In this case, there are essentially no sample uncertainties beside thermal and mechanical vibrations.

When a large number of nano-crystals and macromolecules are employed in measurement, they usually come with a variety of heterogeneities such as size, shape, conformational variability and other disorders due to imperfect processes of sample preparation [12,43,45].

The second type of uncertainties is related to sample delivery including, but not limited to, liquid jets [9], fixed-target arrays [36,66] and goniometer-based approaches [15] in X-ray diffraction. The latter two approaches also enable serial crystallography to be implemented with electron diffraction [7,63].

In a fixed-target approach, for example, a large number of particles are held at known locations on a micro-patterned grid, which is raster-scanned during radiation exposure. Rough features on the wafer surface cause the particles to adopt random orientations, allowing efficient sampling of the Fourier space [9,49].

On the other hand, when liquid jet is used to deliver a stream of micro-sized crystals for X-ray serial crystallography, precise location and orientation information is lost and the resulting diffraction patterns are harder to align [8,9].

The third type of uncertainties has to do with large noise in the measurement data. Low SNR is primarily due to weak interaction with matter in the case of X-ray and low dosage in the case of electron. We will return to the noise issue in Section 10 and carry on with the analysis under the assumption of noiseless data.

The relative orientation between the object and the measurement set-up can be described by the Euler angles between the object frame xyz and the device frame XYZ with Z as the optical axis represented in the object frame by $x(\alpha, \beta)$, $y(\alpha, \beta)$ or $z(\alpha, \beta)$, abstractly denoted by t . The transformation from xyz to XYZ can be described by an intrinsic rotation about the z axis followed by a tilt and an extrinsic rotation about the Z axis (the precession of the object).

In particular, the intrinsic rotation is the key mechanism for providing diverse views of the object in the (regular or random) conical reconstruction methods in cryo-EM which handle the precession by 2D alignment algorithms [24].

There remains the minor ambiguity of the relative displacement of the two frames, resulting in variable off-sets between the two frames from one snapshot to another. The invariance property (29) of an uncoded diffraction pattern will be useful in dealing with the location uncertainty.

In contrast, a coded diffraction pattern is not invariant w.r.t. translation since the random mask breaks the symmetries associated with all rigid motions. But this symmetry-breaking property, when used in proper circumstances, provides complementary advantages to those of an uncoded diffraction pattern as rigorously established in [17].

Let us now introduce the notation for describing the location uncertainty for a given \mathbf{t} . Let $f_{\mathbf{t}}^*$ denote the projection $f_{\mathbf{t}}$ translated by some $\mathbf{l}_{\mathbf{t}} \in \mathbb{Z}^2$, i.e.

$$(36) \quad f_{\mathbf{t}}^*(\mathbf{n}) = f_{\mathbf{t}}(\mathbf{n} + \mathbf{l}_{\mathbf{t}}), \quad \text{subject to } \text{supp}(f_{\mathbf{t}}^*) \subseteq \mathbb{Z}_n^2.$$

We assume that each (coded or uncoded) snapshot is taken for $f_{\mathbf{t}}^*$ (not $f_{\mathbf{t}}$). The invariance property (29) can be restated as

$$(37) \quad |\mathcal{F}(e^{i\kappa f_{\mathbf{t}}})|^2 = |\mathcal{F}(e^{i\kappa f_{\mathbf{t}}^*})|^2.$$

We say that for a given $f \in O_n := \{g : \text{supp}(g) \subseteq \mathbb{Z}_n^3\}$, 3D phase retrieval and PT are *informationally equivalent with respect to \mathcal{T}* if, for a given $f \in O_n$ and any $g \in O_n$, the following two statements are logically equivalent:

$$(38) \quad |\mathcal{F}(\mu \odot e^{i\kappa g_{\mathbf{t}}^*})| = |\mathcal{F}(\mu \odot e^{i\kappa f_{\mathbf{t}}^*})|, \quad \forall \mathbf{t} \in \mathcal{T};$$

$$(39) \quad e^{i\kappa g_{\mathbf{t}}^*} = e^{i\kappa f_{\mathbf{t}}^*}, \quad \forall \mathbf{t} \in \mathcal{T}$$

where $g_{\mathbf{t}}^*$ and $f_{\mathbf{t}}^*$ are defined as in (36). Eq. (39) clearly is equivalent to the phase unwrapping problem:

$$(40) \quad g_{\mathbf{t}}^*(\mathbf{n}) = f_{\mathbf{t}}^*(\mathbf{n}) \quad \text{mod } 2\pi/\kappa, \quad \forall \mathbf{n}, \mathbf{t} \in \mathcal{T}.$$

6. REDUCTION WITH PAIRWISE MEASUREMENTS

To explicitly carry out the reduction to PT under all the uncertainties discussed above, let us consider the measurement scheme stylized in Figure 3 where a beam splitter is inserted behind the object and the mask placed in only one of two light paths behind the splitter. The reader is referred to [38, 40, 51] for recent advances in X-ray splitters.

Our first result is the reduction to projection data per snapshot.

Theorem 6.1. *Let $f \in O_n$ with the singleton $\mathcal{T} = \{\mathbf{t}\}$ for any \mathbf{t} . Consider a random phase mask $\mu(\mathbf{n}) = \exp[i\phi(\mathbf{n})]$ with independent, continuous random variables $\phi(\mathbf{n}) \in \mathbb{R}$. Suppose that for $g \in O_n$, $e^{i\kappa g_{\mathbf{t}}^*}$ produces the same pair of coded and uncoded diffraction patterns as $e^{i\kappa f_{\mathbf{t}}^*}$ (Figure 3), i.e.*

$$(41) \quad |\mathcal{F}(e^{i\kappa g_{\mathbf{t}}^*})|^2 = |\mathcal{F}(e^{i\kappa f_{\mathbf{t}}^*})|^2$$

$$(42) \quad |\mathcal{F}(\mu \odot e^{i\kappa g_{\mathbf{t}}^*})|^2 = |\mathcal{F}(\mu \odot e^{i\kappa f_{\mathbf{t}}^*})|^2$$

Then $e^{i\kappa g_{\mathbf{t}}^} = e^{i\kappa f_{\mathbf{t}}^*}$ almost surely.*

The proof of Theorem 6.1 is given in Appendix A. All the measurement uncertainties are transferred to projection data by phase retrieval with a beam splitter. The presence of a beam splitter facilitates measurement of the physical quantities on the right hand side of (41)-(42) without the information of relative orientation and position of the two frames.

Theorem 6.1 clearly generalizes to an arbitrary \mathcal{T} of any cardinality.

Corollary 6.2. *Theorem 6.1 holds true for any direction set \mathcal{T} .*

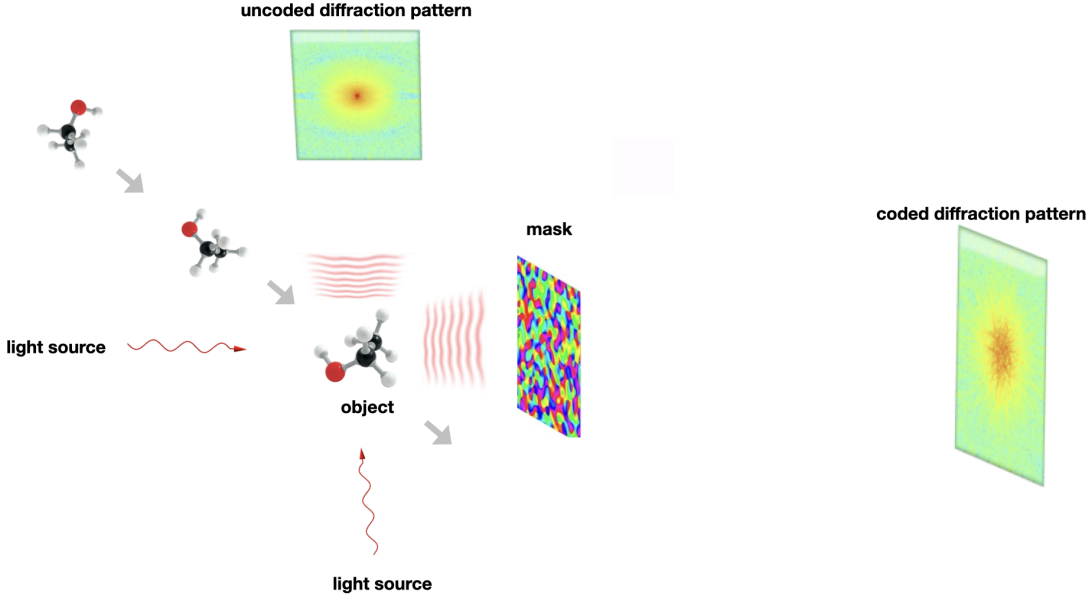


FIGURE 4. Simultaneous illumination of the object with one coded and one uncoded diffraction pattern measured in two directions.

To numerically transform a pair of diffraction patterns to a projection, we can leverage the well established phase retrieval algorithms [22]. See more discussion in Section 10.

To do away with a beam splitter, consider simultaneous illuminations by two beams of directions $\mathbf{t}_0, \mathbf{t}_1$ with only one exit wave masked by the coded aperture as depicted in Figure 4. Both beams' intensities are then measured by detectors at far field. The scheme in Figure 3 is equivalent to the limiting case with $\mathbf{t}_0 = \mathbf{t}_1$.

The scheme in Figure 4 inspires the following result.

Theorem 6.3. *Let $f \in O_n$. Consider a random phase mask $\mu(\mathbf{n}) = \exp[i\phi(\mathbf{n})]$ with independent, continuous random variables $\phi(\mathbf{n}) \in \mathbb{R}$. Suppose that for two directions $\mathbf{t}_0 \neq \mathbf{t}_1$*

$$(43) \quad |\mathcal{F}(e^{i\kappa g_{\mathbf{t}_0}^*})|^2 = |\mathcal{F}(e^{i\kappa f_{\mathbf{t}_0}^*})|^2$$

$$(44) \quad |\mathcal{F}(\mu \odot e^{i\kappa g_{\mathbf{t}}^*})|^2 = |\mathcal{F}(\mu \odot e^{i\kappa f_{\mathbf{t}}^*})|^2$$

Then $e^{i\kappa g_{\mathbf{t}}^} = e^{i\kappa f_{\mathbf{t}}^*}$ almost surely.*

The proof of Theorem 6.3 is given in Appendix B. Instead of a beam splitter, the precise arrangement of the two beams facilitate reconstruction of the projection data by information overlap in the common line. Note that the two beams need not be coherent with each other for the scheme to work since the measurement data are diffraction patterns.

Since a Fourier slice intersects with another slice along a common line, we can generalize Theorem 6.3 as follows.

Corollary 6.4. *Suppose that under the same assumptions in Theorem 6.3, (43) and (44) hold true for $\mathbf{t}_0 \in \mathcal{T}_0$ and $\mathbf{t} \in \mathcal{T}$, respectively, where $|\mathcal{T}_0| \geq 1$. Then $e^{i\kappa g_{\mathbf{t}}^*} = e^{i\kappa f_{\mathbf{t}}^*}$ for all $\mathbf{t} \in \mathcal{T}$ almost surely.*

7. REDUCTION UNDER BORN APPROXIMATION

Under the first-order Born assumption (4) the exit wave is given by

$$(45) \quad v_B(x, y) = 1 - \frac{i}{2\kappa} \int dz' f(x, y, z').$$

At the second stage, the exit wave v_B is multiplied by the mask function μ and then propagates into the far-field as $\mathcal{F}(\mu \cdot v_B)$ where \mathcal{F} is the Fourier transform in the transverse variables. The measured coded diffraction pattern $|\mathcal{F}(\mu \cdot v_B)|^2$ is given by

$$(46) \quad |\mathcal{F}(\mu \cdot v_B)|^2 = |\mathcal{F}(\mu)|^2 + \frac{1}{\kappa} \Im \{ \overline{\mathcal{F}\mu} \cdot \mathcal{F}(\mu \int f dz') \} + \frac{1}{4\kappa^2} |\mathcal{F}(\mu \int f dz')|^2$$

where \Im denotes the imaginary part.

Adopting the dark-field mode of imaging, we use the nonlinear term

$$(47) \quad |\mathcal{F}(\mu \odot f_{\mathbf{t}})|^2, \quad \mathbf{t} \in \mathcal{T},$$

i.e. coded diffraction patterns of the scattered waves, as the basis for reconstruction. With the dataset given by (47), the information equivalence with respect to \mathcal{T} is then defined by the logical equivalence of the following two statements

$$(48) \quad |\mathcal{F}(\mu \odot g_{\mathbf{t}}^*)| = |\mathcal{F}(\mu \odot f_{\mathbf{t}}^*)|, \quad \forall \mathbf{t} \in \mathcal{T};$$

$$(49) \quad g_{\mathbf{t}}^* = e^{i\theta_{\mathbf{t}}} f_{\mathbf{t}}^*, \quad \theta_{\mathbf{t}} \in \mathbb{R}, \quad \forall \mathbf{t} \in \mathcal{T}$$

for a given $f \in O_n$ and any $g \in O_n$.

The following results are analogous to Theorem 6.1, Corollary 6.2, Theorem 6.3 and Corollary 6.4.

Theorem 7.1. *Let $f \in O_n$ with the singleton $\mathcal{T} = \{\mathbf{t}\}$ for any \mathbf{t} . Consider a random phase mask $\mu(\mathbf{n}) = \exp[i\phi(\mathbf{n})]$ with independent, continuous random variables $\phi(\mathbf{n}) \in \mathbb{R}$. Suppose that $\text{supp}(f_{\mathbf{t}})$ is not a subset of a line and that for $g \in O_n$, $g_{\mathbf{t}}^*$ produces the same pair of coded and uncoded diffraction patterns as $f_{\mathbf{t}}^*$, i.e.*

$$(50) \quad |\mathcal{F}(g_{\mathbf{t}}^*)|^2 = |\mathcal{F}(f_{\mathbf{t}}^*)|^2$$

$$(51) \quad |\mathcal{F}(\mu \odot g_{\mathbf{t}}^*)|^2 = |\mathcal{F}(\mu \odot f_{\mathbf{t}}^*)|^2$$

Then $g_{\mathbf{t}}^ = e^{i\theta_{\mathbf{t}}} f_{\mathbf{t}}^*$ for some constant $\theta_{\mathbf{t}} \in \mathbb{R}$.*

The proof of Theorem 7.1 is given in Appendix C.

Corollary 7.2. *Theorem 7.1 holds true for any direction set \mathcal{T} .*

Theorem 7.3. Let $f \in O_n$. Consider a random phase mask $\mu(\mathbf{n}) = \exp[i\phi(\mathbf{n})]$ with independent, continuous random variables $\phi(\mathbf{n}) \in \mathbb{R}$. Suppose that $\text{supp}(f_{\mathbf{t}})$ is not a subset of a line and that for $g \in O_n$

$$(52) \quad |\mathcal{F}(g_{\mathbf{t}_0}^*)|^2 = |\mathcal{F}(f_{\mathbf{t}_0}^*)|^2$$

$$(53) \quad |\mathcal{F}(\mu \odot g_{\mathbf{t}}^*)|^2 = |\mathcal{F}(\mu \odot f_{\mathbf{t}}^*)|^2$$

for $\mathbf{t}_0 \neq \mathbf{t}$. Then $g_{\mathbf{t}}^* = e^{i\theta_{\mathbf{t}}} f_{\mathbf{t}}^*$ for some constant $\theta_{\mathbf{t}} \in \mathbb{R}$.

The proof of Theorem 7.3 is given in Appendix D.

Corollary 7.4. Suppose that under the same assumptions in Theorem 7.3, (52) and (53) hold true for $\mathbf{t}_0 \in \mathcal{T}_0$ and $\mathbf{t} \in \mathcal{T}$, respectively, where $|\mathcal{T}_0| \geq 1$. Then $g_{\mathbf{t}}^* = e^{i\theta_{\mathbf{t}}} f_{\mathbf{t}}^*$ for all $\mathbf{t} \in \mathcal{T}$ almost surely.

7.1. Sector constraint. X-rays interact rather weakly with matter so the complex refractive index is often denoted as

$$(54) \quad n = 1 - \delta - i\beta, \quad 0 < |\delta|, \beta \ll 1,$$

where the real part of the refractive index is often less than 1 (i.e. $\delta > 0$) and the imaginary part β is the absorption coefficient.

By (3) and (54),

$$(55) \quad f = \frac{1}{2}(n^2 - 1) \approx -\delta - i\beta$$

and hence $f_{\mathbf{t}}$ satisfies the so called sector condition introduced in [17], i.e.

$$(56) \quad \angle f_{\mathbf{t}}(\mathbf{n}) \in [a, b], \quad |a - b| < 2\pi,$$

for all $\mathbf{n} \in \mathbb{Z}_2^3$, where a and b are two constants independent of \mathbf{n} ($a = -\pi, b = 0$ in the case of $\beta > 0$). Moreover, for X-ray at wavelength 1\AA , β is typically much smaller than $\delta > 0$ resulting in a very narrow sector about the negative real axis.

The sector condition (56) enables reduction without the uncoded diffraction pattern (43).

Theorem 7.5. [17] Let $f \in O_n$ with the singleton $\mathcal{T} = \{\mathbf{t}\}$ for any \mathbf{t} and satisfy the sector condition (56). Consider a random phase mask $\mu(\mathbf{n}) = \exp[i\phi(\mathbf{n})]$ with independent uniform random variables $\phi(\mathbf{n})$ over $[0, 2\pi]$. Suppose that $\text{supp}(f_{\mathbf{t}})$ is not a subset of a line and that for $g \in O_n$, $g_{\mathbf{t}}^*$ produces the same coded diffraction pattern as $f_{\mathbf{t}}^*$. Then with probability at least

$$(57) \quad 1 - n^2 \left| \frac{b - a}{2\pi} \right|^{\lfloor S_{\mathbf{t}}/2 \rfloor}$$

$g_{\mathbf{t}}^* = e^{i\theta_{\mathbf{t}}} f_{\mathbf{t}}^*$ for some constant $\theta_{\mathbf{t}} \in \mathbb{R}$ where $S_{\mathbf{t}}$ is the number of nonzero pixels of $f_{\mathbf{t}}$.

Corollary 7.6. Theorem 7.5 holds true for any direction set \mathcal{T} with probability at least

$$(58) \quad \prod_{\mathbf{t} \in \mathcal{T}} \left(1 - n^2 \left| \frac{b - a}{2\pi} \right|^{\lfloor S_{\mathbf{t}}/2 \rfloor} \right).$$

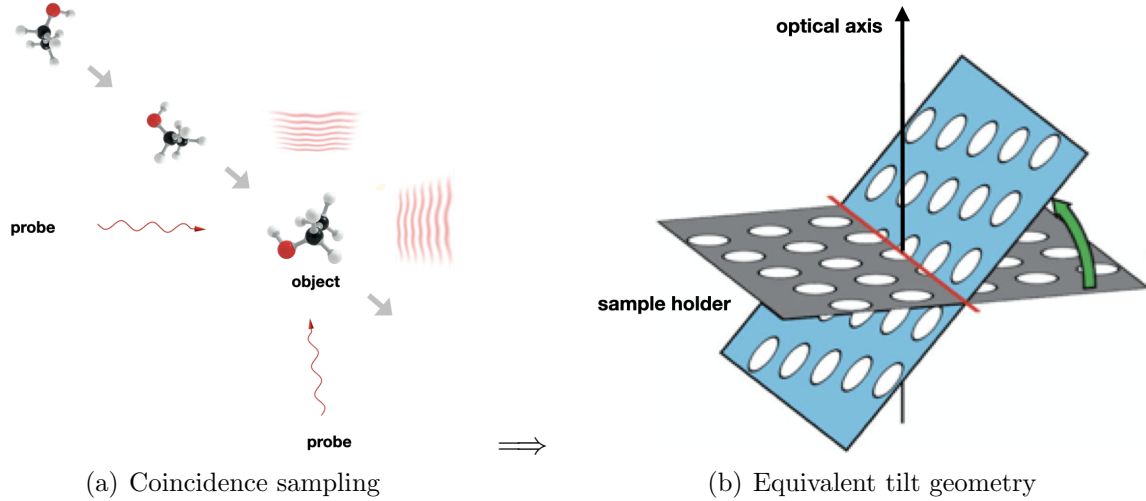


FIGURE 5. Coincident data collection implemented by the random conical tilt and orthogonal tilt in cryo-EM both of which collect **pairs** of measurement data of a fixed relative orientation corresponding to the angle about 50 deg and 90 deg, respectively, between the two beams [24, 39].

The sector constraint (56) can be readily incorporated in phase retrieval algorithms and the resulting performance improves with a narrower sector as already indicated in the probability estimate (57) [19].

8. RANDOM CONICAL TILT AND ORTHOGONAL TILT

The main idea in Figure 4 can be realized in a different way with a fixed-target sample delivery by the scheme *random conical tilt* (RCT) or *orthogonal tilt* (OT) commonly used in cryo-EM. Both schemes collect **pairs** of measurement data of fixed relative orientations [24, 39].

In a fixed-target approach, samples mounted on solid supports are raster-scanned through the beam. To achieve high hit rates and consistently produce diffraction patterns, the sample support should ideally be periodically structured and present the samples at known and well-defined positions [57].

As shown in Figure 5 (b), many particles are randomly located and oriented on a grid which can be precisely tilted about a tilt axis by a goniometer. With dose-fractionated beams, the diffraction patterns of the same particles in the two orientations are measured with *coded and uncoded* apertures in correspondence with Figure 4.

The main difference between the schemes of Figure 4 and Figure 5(b) is that in the former approach the diffraction-before-destruction idea is implemented with two coincident beams with SNR limited only by the intensities of femtosecond XFEL pulses whereas in the latter a maximal radiation dose has to be fractionated resulting in smaller radiation-damage-limited SNR. With $10^4 - 10^6$ times stronger scattering cross section and 10^3 times weaker radiation damage per scattering, electron diffraction is better suited for the implementation of RCT and OT.

These caveats aside, Corollary 6.4 and 7.4 can be modified as follows.

Corollary 8.1. *Let \mathcal{T}_0 and \mathcal{T} in Corollary 6.4 and 7.4 be the set of directions in the object frame of the particles on the sample grid in the two tilt positions, respectively. Then, under the Rytov and Born approximations, respectively*

$$(59) \quad e^{i\kappa g_t^*} = e^{i\kappa f_t^*}$$

$$(60) \quad g_t^* = e^{i\theta_t} f_t^* \quad \text{for some constant } \theta_t \in \mathbb{R},$$

for all $t \in \mathcal{T}$ almost surely.

9. PHASE UNWRAPPING

For each projection considered separately in (40), there are an infinite number of solutions of 2D phase unwrapping. What type of schemes \mathcal{T} would guarantee that the unwrapped phase in 3D can be uniquely determined (i.e. $g(\mathbf{n}) = f(\mathbf{n}), \forall \mathbf{n} \in \mathbb{Z}_n^3$)?

A simple approach is based on the continuity of the projection's dependence on the direction t . For simplicity of presentation, let us assume $f_t^* = f_t, g_t^* = g_t$, i.e. $l_t = 0$ for all $t \in \mathcal{T}$ in (36).

Let \mathcal{T}_ϵ denote the graph with the nodes given by $t \in \mathcal{T}$ and the edges defined between any two nodes $t_1, t_2 \in \mathcal{T}$ such that $|\angle t_1 t_2| \leq \epsilon$ (such edges are called ϵ -edges). We call \mathcal{T} is ϵ -connected if \mathcal{T}_ϵ is a connected graph. We say that two nodes t_1, t_2 are ϵ -connected if there is an ϵ -edge between them.

Suppose that \mathcal{T} is ϵ -connected for certain ϵ (to be determined later). The continuous dependence of g_t, f_t on t implies that $g_{t_1} - g_{t_2}$ and $f_{t_1} - f_{t_2}$ are small if $\angle t_1 t_2$ is sufficiently small. On the other hand, $h_{t_1} - h_{t_2}$ is an integer multiple of $2\pi/\kappa$ where $h_t := g_t - f_t$. Then for ϵ -connected \mathcal{T} , $h_t(\mathbf{n})$ is a constant for each \mathbf{n} and hence $g_t - f_t$ is independent of t . A rough calculation gives the estimate $\mathcal{O}(1/n)$ for the needed closeness ϵ of two adjacent projections.

Example 9.1. Consider the following set of projections:

$$(61) \quad \{(1, \alpha_l, \beta_l) : l = 1, \dots, n\} \cup \{(0, \alpha_0, \beta_0), (0, 0, 1)\}$$

with the property that $|\alpha_0, \beta_0| \neq 0$ and $\{\alpha_l \eta + \beta_l \zeta : l = 1, \dots, n\}$ has n distinct members for any fixed pair $(\eta, \zeta) \neq (0, 0)$.

Suppose that (40) holds true with $h_t := g_t - f_t$ being independent of t in (61). Namely, for $t = (1, \alpha, \beta)$ and some $c(\cdot, \cdot)$ independent of α, β ,

$$(62) \quad \widehat{h}_{x(\alpha, \beta)}(j, k) = c(j, k)$$

and hence by Fourier Slice Theorem

$$(63) \quad \widehat{h}(-\alpha j - \beta k, j, k) = c(j, k)$$

for $j, k \in \mathbb{Z}_p$.

Let

$$(64) \quad \widehat{h}(\xi, \eta, \zeta) = \sum_m \widehat{h}_{\eta\zeta}(m) e^{-2\pi i m \xi / p}$$

with

$$(65) \quad \widehat{h}_{\eta\zeta}(m) = \sum_l \widehat{h}_\eta(m, l) e^{-2\pi i l \zeta / p}$$

and

$$(66) \quad \widehat{h}_\eta(m, l) = \sum_k h(m, k, l) e^{-2\pi i k \eta / p}.$$

By the support constraint $\text{supp}(h) \in \mathbb{Z}_n^3$, (63)-(64) becomes the $n \times n$ Vandermonde system

$$(67) \quad V \widehat{h}_{\eta\zeta} = \begin{bmatrix} c(\eta, \zeta) \\ c(\eta, \zeta) \\ \vdots \\ c(\eta, \zeta) \end{bmatrix}$$

with the all-one vector $\mathbb{1}$ and

$$(68) \quad V = [V_{ij}], \quad V_{ij} = e^{-2\pi i \xi_i j / p}, \quad \xi_i = -\alpha_i \eta - \beta_i \zeta$$

for $\{\alpha_i, \beta_i : i = 1, \dots, n\}$. The Vandermonde system is nonsingular if and only if $\{\xi_i : i = 1, \dots, n\}$ has n distinct members.

Since the system (67) has a unique solution, we identify $\widehat{h}_{\eta\zeta}(\cdot)$ as

$$\widehat{h}_{\eta\zeta}(\cdot) = c(\eta, \zeta) \delta(\cdot).$$

For $m \neq 0$, $\widehat{h}_{\eta\zeta}(m) = 0$ for all η, ζ and hence $\widehat{h}_\eta(m, l) = 0$ for all l and $m \neq 0$. Likewise for (66), we select n distinct values of η to perform inversion of the Vandermonde system and obtain

$$(69) \quad h(m, k, l) = 0, \quad m \neq 0.$$

In other words, h is supported on the (y, z) plane. Consequently the projection of h in the direction of $(0, \alpha_0, \beta_0)$ would be part of a line segment and, hence by the assumption of h_t 's independence of $\mathbf{t} = (1, \alpha_l, \beta_l), l = 1, \dots, n$, h_t is also a line object for all these directions.

That is to say, h is supported on the z -axis. Now that $(0, 0, 1) \in \mathcal{T}$, the projection of h in $(0, 0, 1)$ is Kronecker's delta function δ at the origin and hence, for some $\ell \in \mathbb{Z}$,

$$(70) \quad g(\mathbf{n}) - f(\mathbf{n}) = \frac{2\pi}{\kappa} \ell \delta(\mathbf{n})$$

where δ is Kronecker's delta function at the origin.

The ambiguity on the right hand side of (70) can be further eliminated by limiting the maximum variation of the object between two adjacent grid points to less than π/κ . This will also lead to an explicit upper bound on ϵ but here we will content ourselves with the rough bound $\epsilon = \mathcal{O}(1/n)$.

Collecting and extending the above analysis, we obtain the next result.

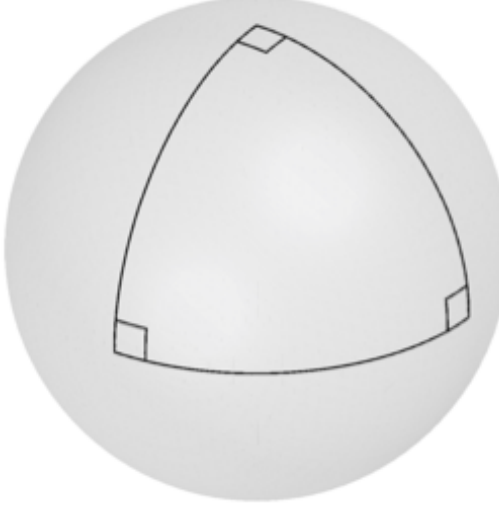


FIGURE 6. A sphere representing all projection directions in the object frame. Any *two* of the three great circular arcs, when sufficiently sampled, provide enough information for unwrapping the object phases (cf. (72) with $\alpha = 0$). This is an example of dual-axis tilting, each of range $\pi/2$.

Theorem 9.2. *Let \mathcal{T} be a ϵ -connected scheme containing any one of the following three sets of projections:*

- (x) $\{(1, \alpha_l, \beta_l) : l = 1, \dots, n\} \cup \{(0, 1, \beta_0), (0, 0, 1)\}$
- (y) $\{(\beta_l, 1, \alpha_l) : l = 1, \dots, n\} \cup \{(\beta_0, 0, 1), (1, 0, 0)\}$
- (z) $\{(\alpha_l, \beta_l, 1) : l = 1, \dots, n\} \cup \{(1, \beta_0, 0), (0, 1, 0)\}$

with the property that

$$(71) \quad \{\alpha_l \xi + \beta_l \eta : |\alpha_l|, |\beta_l| < 1, l = 1, \dots, n\} \text{ has } n \text{ distinct elements for each } (\xi, \eta) \neq (0, 0).$$

Suppose that the maximum variation of the object f between two adjacent grid points is less than π/κ and (40) holds for a sufficiently small $\epsilon = \mathcal{O}(1/n)$. Then $g = f$.

Since $|\alpha_l|, |\beta_l| < 1$, none of the schemes (x), (y), (z), alone can be ϵ -connected (for sufficiently small ϵ), but some combination of the three can as shown by the following explicit scheme:

$$(72) \quad \mathcal{T} = \{(1, \frac{l}{q}, \alpha), (\frac{l}{q}, 1, \alpha), (0, 1, \frac{l}{q}), (0, \frac{l}{q}, 1) : l = 0, \dots, q\}$$

with q sufficiently large and fixed $|\alpha| < 1$. By the symmetry of projection, we may assume $\alpha \geq 0$. The family of $\mathbf{t} \in \mathcal{T}$ moves along a latitude for a range $\pi/2$ from $(1, 0, \alpha)$ to $(0, 1, \alpha)$ and then along a longitude for a range $\arccos(\alpha)$ to $(0, 0, 1)$ (see Figure 6 for $\alpha = 0$) where $\arccos(\alpha) > \pi/4$ since $\alpha < 1$.

The scheme (72) is a combination of a conical tilting (the latitudinal movement above) of range $\pi/2$ at any conical angle $\tau \in (\pi/4, \pi/2]$ and an orthogonal single-axis tilting (the longitudinal movement above) of range τ . Single-axis tilting (maximal range π due to the symmetry of projection) and conical tilting (maximal range 2π) are two most widely used

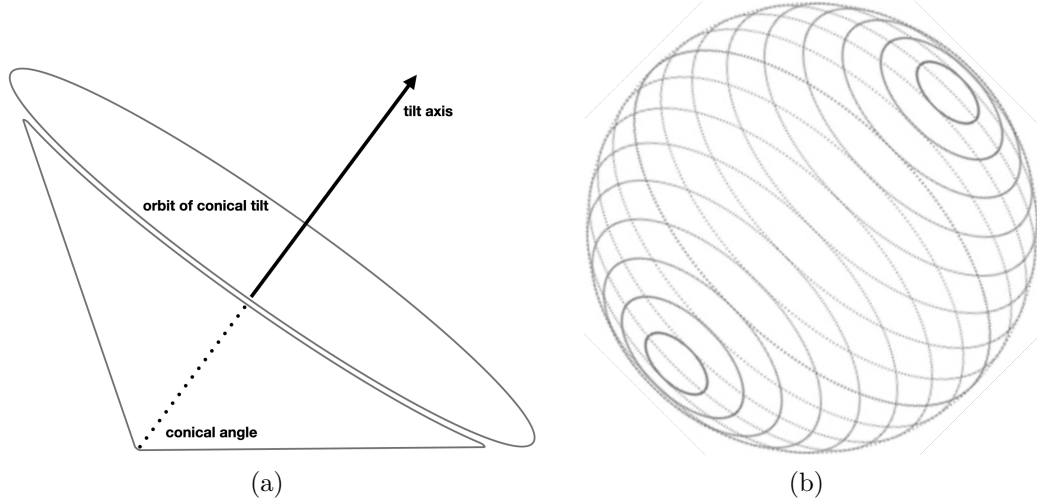


FIGURE 7. (a) Geometry of conical tilt. A single-axis tilt orbit is a great circle, corresponding to a conical angle $\pi/2$; (b) Conical tilts about an axis of obliquity may be parametrized as in Theorem 9.2.

data collection schemes in cryo-EM [24]. When $\tau = \pi/2$, the combination becomes an orthogonal dual-axis tilting of a tilt range $\pi/2$ for each axis (Figure 6).

More conveniently, instead of being split into a conical tilting and a single-axis tilting, the schemes in Theorem 9.2 can be implemented as one conical tilting of range π with the tilt axis, say pointing at $(1, 1, 1)$, and a conical angle *slightly greater than* $\pi/4$ (Figure 7).

On the other hand, single-axis tilting (corresponding to conical angle $\pi/2$) is not covered by Theorem 9.2 and contains certain blindspot as exhibited in Example 9.1. This can be remedied by another single-axis tilting as shown in Figure 6 which is an example of a dual-axis tilting with the tilt range $\pi/2$ for each axis [50].

In summary, we have identified three sampling schemes that can be conveniently implemented to unwrap phases under the guarantee of Theorem 9.2:

- A conical tilting of range π at a conical angle slightly greater than $\pi/4$ (or slightly smaller than $3\pi/4$);
- An orthogonal dual-axis tilting of a tilt range at least $\pi/2$ for each axis;
- A combination of a conical tilting of range at least $\pi/2$ at any conical angle $\tau \in (\pi/4, \pi/2]$ and an orthogonal single-axis tilting of a tilt range at least τ .

10. CONCLUSIONS AND DISCUSSION

3D phase retrieval is a form of ptychography by rotations instead of by shifts as in standard ptychography. The key to any form of ptychography is information redundancy, which in this case lies in the common lines between any pairs of Fourier slices (Corollary 6.4 and 7.4).

To this end, the coded aperture leverages the information redundancy by spreading the shared information across the two intersecting Fourier slices. In particular, this enables the reduction from diffraction data to projection data for the data collection schemes of random conical tilt and orthogonal tilt if performed with coded and uncoded apertures (Corollary 8.1) as well as effective initialization methods for reconstruction [11, 21].

With the introduction of a beam splitter (Theorem 6.1 and 7.1), the information overlap further extends from a common line to that of the whole Fourier slice with improved performance in resolution and noise stability. Moreover, the coded aperture can be simultaneously calibrated with the object by effective algorithms [18, 20, 22].

Effective algorithms for implementing the schemes of Theorem 6.1 and 7.1 are based on the following two projection operators: The first is \mathcal{P}_1 unto the range space of the matrix

$$(73) \quad A = \begin{bmatrix} \Phi \operatorname{diag}\{\mu\} \\ \Phi \end{bmatrix}.$$

where Φ is the $p^2 \times n^2$ oversampled Fourier matrix; the second is \mathcal{P}_2 unto the $2p^2$ -dim torus defined by the diffraction pattern data:

$$\mathcal{Y} := \{y \in \mathbb{C}^{2p^2} : |y|^2 = d\}$$

where d is the vectorized data consisting of coded and uncoded diffraction patterns. The former is explicitly given by $\mathcal{P}_1 = AA^\dagger$ where A^\dagger is the pseudo-inverse of A and the latter

$$(74) \quad \mathcal{P}_2 z = \sqrt{d} \odot \operatorname{sgn}(z), \quad z \in \mathbb{C}^{2p^2}$$

where $\operatorname{sgn}(z)$ is the phase factor vector of z [21].

For reconstruction in the setting of Theorem 7.5, \mathcal{P}_2 is the same as (74) but $\mathcal{P}_1 = AA^\dagger \mathcal{P}_0$ where $A = \Phi \operatorname{diag}\{\mu\}$ and \mathcal{P}_0 the real-space projection unto the sector constraint (see [19] and references therein).

With the measurement scheme in Figure 3, 4 and 5, diffraction patterns can be converted into projections without the knowledge of relative orientations and locations between the object and device frames, enabling classification and alignment by techniques developed for single-particle cryo-EM such as the common-line methods [59, 61], the maximum-likelihood methods [42, 58] and the Bayesian methods [53–55].

In particular, the Bayesian methods have a greater capability for mitigating noise than the common-lines based techniques, which require a high SNR dataset to work [24], and play an important role in cryo-EM’s reaching the milestone of atomic resolution [13]. With everything else being equal, the Bayesian methods applied to projection data [53–55] are expected to outperform those applied to diffraction patterns [25, 41].

We show that 3D phase unwrapping can be achieved with three readily implementable schemes (Theorem 9.2): (i) The conical tilting of range π at a conical angle slightly greater than $\pi/4$; (ii) The orthogonal dual-axis tilting of a tilt range at least $\pi/2$ for each axis; (iii) A combination of a conical tilting of range at least $\pi/2$ at any conical angle $\tau \in (\pi/4, \pi/2]$ and an orthogonal single-axis tilting of a tilt range at least τ .

Note that the minimum total radiation dose for each scheme is proportional to the scheme's minimum total length, which is, respectively, $\pi/\sqrt{2}$, π and $\frac{1}{2}(1+1/\sqrt{2})\pi$ for scheme (i), (ii) and (iii).

It is also interesting to compare the phase unwrapping conditions of Theorem 9.2 with Orlov's condition that the continuous sampling orbit intersects any great circle on the unit sphere. Orlov's condition is the necessary and sufficient condition for the existence of a unique solution by the method of filtered back propagation (FBP) for 3D projection tomography under the Born approximation (thus no wrapped phases) [16]. Notably, among the three phase unwrapping schemes above, only scheme (ii) satisfies Orlov's condition. In contrast, while a single-axis tilting of tilt range π satisfies Orlov's condition by itself, it can not unambiguously unwrap the phases in general.

Let us turn to the noise issue not explicitly addressed by our results.

For example, given a noisy data set of diffraction patterns at a certain SNR, what would be the corresponding SNR of the data set of the resulting projection tomography? How many snapshots are needed to overcome the measurement noise and uncertainties?

The first question has as much to do with the reconstruction method as the information content of the datasets. Our previous numerical studies suggest plausible noisy information equivalence in the sense that the reconstructed projection dataset under the Born approximation has comparable SNRs (noise amplification factor close to 1 for SNR down to about 2) [11, 22]. This is eventually tenable since the SNR of the diffraction-before-destruction approach is limited only by the intensities of femtosecond X-ray pulses which can be continuously amplified as XFEL technologies progress.

For the second question above, consider 3D projection tomography at low SNR. Depending on the sampling geometry but with full knowledge of it, SNR in 3D projection tomography under the Born approximation with Poisson noise is estimated to be about twice the square root of the ratio of the mean total number of scattered photons detected during the scan and the total number of spatially resolved voxels [30].

Currently about 100 X-ray photons or similar order of magnitude are scattered from a single molecule per snapshot, so reconstructing a volume of, say 10^6 voxels at $\text{SNR} = 2$ in single-molecule 3D projection tomography requires at least 10^4 snapshots. Many more snapshots will be needed with the current form of serial crystallography whose datasets consist primarily of uncoded diffraction patterns.

Nevertheless, a large number of extremely noisy snapshots suggests an alternative, likely better approach to data processing. Instead of reconstructing the projection data from each pair of diffraction patterns as suggested at the beginning of Section 10, one can process the whole dataset of coupled coded and uncoded diffraction patterns together to achieve orientation alignment and object reconstruction simultaneously, for which Corollary 6.2, 6.4, 7.2, 7.4 and 7.6 provide a theoretical basis. This will be our future work of research.

ACKNOWLEDGMENTS

The research is supported by the Simons Foundation grant FDN 2019-24 and the NSF grant CCF-1934568.

REFERENCES

- [1] A. Averbuch & Y. Shkolnisky, “3D discrete X-ray transform,” *Appl. Comput. Harmon. Anal.* **17** (2004) 259-276.
- [2] A. Barty, J. Küpper, H. N. Chapman, “Molecular imaging using X-ray free-electron lasers,” *Annu. Rev. Phys. Chem.* **64** (2013), 415-435.
- [3] P. Baum, “On the physics of ultrashort single-electron pulses for time-resolved microscopy and diffraction,” *Chem. Phys.* **423** (2013) 55-61.
- [4] W. T. Baxter, R. A. Grassucci, H. Gao, J. Frank, “Determination of signal-to-noise ratios and spectral SNRs in cryo-EM low-dose imaging of molecules,” *J. Struct. Biol.* **166** (2009) 126-132.
- [5] T. Bendory, A. Bartesaghi and A. Singer, “Single-particle cryo-electron microscopy,” *IEEE Sign. Proc. Mag.* March 2020, 58-76.
- [6] S. Boutet *et al.* “High-resolution protein structure determination by serial femtosecond crystallography”. *Science* **337**(2012), 362-364.
- [7] R. Bückner, P. Hogan-Lamarre, P. Mehrabi, E. C. Schulz, L. A. Bultema, Y. Gevorkov, W. Brehm, O. Yefanov, D. Oberthür, G. H. Kassier & R.J. D. Miller, “Serial protein crystallography in an electron microscope”, *Nat. Commun.* **11** (2020) 996.
- [8] H. N. Chapman, “Femtosecond X-ray protein nanocrystallography,” *Nature* **470** (2011) 73-77.
- [9] L. M. G. Chavas, L. Gumprecht and H. N. Chapman, “Possibilities for serial femtosecond crystallography sample delivery at future light sources”, *Struct. Dyn.* **2** (2015), 041709.
- [10] B. Chen and J.J. Stamnes, “Validity of diffraction tomography based on the first Born and the first Rytov approximations,” *Appl. Opt.* **37** (1998), 2996-3006.
- [11] P. Chen, A. Fannjiang, G. Liu, “Phase retrieval with one or two diffraction patterns by alternating projections of the null vector,” *J. Fourier Anal. Appl.* **24** (2018), 719-758.
- [12] J. P. J. Chen, J. C. H. Spence and R. P. Millane, “Direct phasing in femtosecond nanocrystallography. I. Diffraction characteristics,” *Acta Cryst. A* **70** (2014) 143-153.
- [13] Y. Cheng, “Single-particle cryo-EM – How did it get here and where will it go,” *Science* **361** (2018) 876-880.
- [14] M. T. B. Clabbers and J. P. Abrahams, “Electron diffraction and three-dimensional crystallography for structural biology,” *Crystallogr. Rev.* **24** (2018) 176-204.
- [15] A. E. Cohen *et. al* “Goniometer-based femtosecond crystallography with X-ray free electron lasers,” *Proc. Natl. Acad. Sci. USA* **111** (2014) 17122-17127.
- [16] M. Defrise, R. Clack and D. Townsend, “Solution to the three-dimensional image reconstruction problem from two-dimensional parallel projections,” *J. Opt. Soc. Am. A* **10** (1995) 869-877.
- [17] A. Fannjiang, “Absolute uniqueness of phase retrieval with random illumination,” *Inverse Problems* **28** (2012), 075008.
- [18] A. Fannjiang & P. Chen, “Blind Ptychography: uniqueness and ambiguities,” *Inverse Problems* **36** (2020) 045005.
- [19] A. Fannjiang and W. Liao, “Phase retrieval with random phase illumination,” *J. Opt. Soc. Am. A* **29** (2012), 1847-1859. Code download: <https://www.math.ucdavis.edu/~fannjiang/home/codes/RPICode/>
- [20] A. Fannjiang and W. Liao, “Fourier phasing with phase-uncertain mask,” *Inverse Problems* **29** (2013) 125001. Code download: <https://www.math.ucdavis.edu/~fannjiang/home/codes/PUMcode/>
- [21] A. Fannjiang and T. Strohmer, “The numerics of phase retrieval,” *Acta Num.* **29** (2020), 125-228.
- [22] A. Fannjiang and Z. Zhang, “Fixed point analysis of Douglas-Rachford Splitting for ptychography and phase retrieval,” *SIAM J. Imaging Sci.* **13** (2020), 609-650. Code download: https://github.com/AnotherdayBeaux/Blind_Ptychography_GUI.
- [23] A.R. Faruqi, R. Henderson, G. McMullan, “Progress and development of direct detectors for electron cryomicroscopy,” *Adv. Imaging Electron Phys.* **190** (2015), 103-141.
- [24] J. Frank, *Three-Dimensional Electron Microscopy of Macromolecular Assemblies*, 2nd edition, Oxford University Press, 2006.

- [25] R. Fung, V. L. Shneerson, D. K. Saldin, and A. Ourmazd, “Structure from fleeting illumination of faint spinning objects in flight,” *Nature Phys.* **5** (2009), 64-67.
- [26] M. Gemmi, E. Mugnaioli, T. E. Gorelik, U. Kolb, L. Palatinus, P. Boullay, S. Hovmöller, and J. P. Abrahams, “3D electron diffraction: The nanocrystallography revolution,” *ACS Central Science* **5** (8) (2019), 1315-1329.
- [27] D. Giannakis, P. Schwander, A. Ourmazd, “The symmetries of image formation by scattering. I. Theoretical framework,” *Opt. Exp.* **20** (2012) 12799-12826.
- [28] A. Gorel, I. Schlichting and T. R. M. Barends, “Discerning best practices in XFEL-based biological crystallography – standards for nonstandard experiments,” *IUCrJ* **8** (2021) 532-543.
- [29] T. E. Gureyev, T.J. Davis, A. Pogany, S.C. Mayo and S.W. Wilkins, “Optical phase retrieval by use of first Born- and Rytov-type approximations,” *Appl. Opt.* **43** (2004) 2418-2430.
- [30] T. E. Gureyev, A. Kozlov, Y. I. Nesterets, D. M. Paganin, A. V. Martin and H. M. Quiney, “Signal-to-noise, spatial resolution and information capacity of coherent diffraction imaging,” *IUCrJ* **5** (2018) 716-726.
- [31] P.W. Hawkes and E. Kasper, “*Principles of Electron Optics, Vol. 3: Wave Optics*. Academic Press, London, 1994.
- [32] R. Henderson, “The potential and limitations of neutrons, electrons and X-rays for atomic resolution microscopy of unstained biological molecules,” *Q. Rev. Biophys.* **28** (1995), 171-193.
- [33] J. M. Holton and K.A. Frankel, “The minimum crystal size needed for a complete diffraction data set,” *Acta Cryst. D* **66** (2010) 393-408.
- [34] X. Huang, H. Miao, J. Steinbrener, J. Nelson, D. Shapiro, A. Stewart, J. Turner and C. Jacobsen, “Signal-to-noise and radiation exposure considerations in conventional and diffraction x-ray microscopy,” *Opt. Exp.* **17** (2009) 13541-13553.
- [35] G. Huldt, A. Szoke, and J. Hajdu, “Diffraction imaging of single particles and biomolecules,” *J. Struct. Biol.* **144** (2003), 219-227.
- [36] Y. Inokuma, S. Yoshioka, J. Ariyoshi, T. Arai, Y. Hitora, K. Takada, S. Matsunaga, K. Rissanen & M. Fujita, “X-ray analysis on the nanogram to microgram scale using porous complexes,” *Nature* **495** (2013) 461- 466.
- [37] L. C. Johansson, B. Stauch, A. Ishchenko and V. Cherezov, “A bright future for serial femtosecond crystallography with XFELs,” *Trends Biochem. Sci.* **42** (2017) 749-762.
- [38] M. Lebugle, G. Seniutinas, F. Marschall, V.A. Guzenko, D. Grolimund and C. David, ““Tunable kinoform x-ray beam splitter,” *Opt. Lett.* **42** (2017) 4327-4330.
- [39] A. Leschziner, “The orthogonal tilt reconstruction method,” *Methods in Enzymology* **482** (2010), 237-262.
- [40] K. Li, Y. Liu, M. Seaberg, M. Chollet, T. M. Weiss, and A. Sakdinawat, “Wavefront preserving and high efficiency diamond grating beam splitter for x-ray free electron laser,” *Opt. Exp.* **28** (2020), 10939-10950.
- [41] N.D. Loh and V. Elser, “Reconstruction algorithms for single-particle diffraction imaging experiments,” *Phys. Rev. E* **80** (2009) 6705.
- [42] Lyumkis, D., Brilot, A.F., Theobald, D.L., and Grigorieff, N. “Likelihood-based classification of cryo-EM images using FREALIGN.” *J. Struct. Biol.* **183** (2013), 377-388.
- [43] M. Metz, R.D. Arnal, W. Brehm, H. N. Chapman, A. J. Morgan and R. P. Millane, “Macromolecular phasing using diffraction from multiple crystal forms”, *Acta Cryst. A* **77** (2021), 19-35.
- [44] R. P. Millane, “Phase retrieval in crystallography and optics,” *J. Opt. Soc. Am. A* **7** (1990) 394-411.
- [45] A. J. Morgan, K. Ayyer, A. Barty, J. P. J. Chen, T. Ekeberg, D. Oberthuer, T. A. White, O. Yefanova and H. N. Chapman, “*Ab initio* phasing of the diffraction of crystals with translational disorder,” *Acta Cryst. A* **75** (2019), 25-40.
- [46] F. Natterer, *The Mathematics of Computerized Tomography*, SIAM, 2001.
- [47] Nannenga BL, Gonen T. “The cryo-EM method microcrystal electron diffraction (MicroED)”. *Nat Methods* **16** (2019), 369-379.
- [48] D. Oberthür, “Biological single-particle imaging using XFELs - towards the next resolution revolution,” *IUCrJ* **5** (2018) 663-666.

- [49] R. L. Owen, D. Axford, D. A. Sherrell, A. Kuo, O. P. Ernst, E. C. Schulz, R. J. D. Miller, and H. M. Mueller-Werkmeister, “Low-dose fixed-target serial synchrotron crystallography,” *Acta Cryst. D Struct. Biol.* **73** (2017), 373-378.
- [50] P. Penczek, M. Marko, K. Buttle and J. Frank, “Double-tilt electron tomography,” *Ultramicroscopy* **60** (1995) 393-410.
- [51] S. Reiche, G. Knopp, B. Pedrini, E. Prat, G. Aeppli and S. Gerber “A perfect X-ray beam splitter and its applications to time-domain interferometry and quantum optics exploiting free-electron lasers.” *Proc. Natl. Acad. Sci. U.S.A.* **119** (2022), e2117906119.
- [52] S. M. Rytov, “Diffraction of light by ultrasonic waves,” *Izvestiya Akademii Nauk SSSR, Seriya Fizicheskaya (Bulletin of the Academy of Sciences of the USSR, Physical Series)* **2** (1937) 223-259.
- [53] M. Samso, M.J. Palumbo, M. Radermacher, J.S. Liu and C.E. Lawrence, “A Bayesian method for classification of images from electron micrographs.” *J. Struct. Biol.* **138** (2002), 157-170.
- [54] S. H. W. Scheres, “A Bayesian view on cryo-EM structure determination,” *J. Mol. Biol.* **415** (2012), 406-418.
- [55] S.H. W. Scheres, “RELIION: implementation of a Bayesian approach to cryo-EM structure determination.” *J. Struct. Biol.* **180** (2012), 519-530.
- [56] V. L. Shneerson, A. Ourmazd and D. K. Saldin, “Crystallography without crystals. I. The common-line method for assembling a three-dimensional diffraction volume from single-particle scattering.” *Acta Cryst. A* **44** (2008), 303-315.
- [57] R. G. Sierra, U. Weierstall, D. Oberthuer, M. Sugahara, E. Nango, S. Iwata, and A. Meents, “Sample delivery techniques for serial crystallography,” in *X-Ray Free Electron Lasers - A Revolution in Structural Biology*, S. Boutet, P. Fromme and M. S. Hunter (eds), Springer Nature, Switzerland, 2018.
- [58] F.J. Sigworth, “A maximum-likelihood approach to single-particle image refinement,” *J. Struct. Biol.* **122** (1998), 328-339.
- [59] A. Singer and Y. Shkolnisky, “Three-dimensional structure determination from common lines in cryo-EM by eigenvectors and semidefinite programming,” *SIAM J. Imag. Sci.* **4** (2011) 543-572.
- [60] Sui, S., Wang, Y., Kolewe, K. W., Srager, V., Henning, R., Schiffman, J. D., et al. “Graphene-based microfluidics for serial crystallography.” *Lab on a Chip* **16** (2016), 3082-3096.
- [61] M. van Heel, “Angular reconstitution: a posteriori assignment of projection directions for 3D reconstruction.” *Ultramicroscopy* **21**, 111-124.
- [62] Lutz Waldecker, Roman Bertoni, and Ralph Ernstorfer, “Compact femtosecond electron diffractometer with 100 keV electron bunches approaching the single-electron pulse duration limit,” *J. Appl. Phys.* **117** (2015), 044903.
- [63] J. T.C. Wennmacher, C. Zaubitzer, T. Li, Y. K. Bahk, J. Wang, J. A. van Bokhoven & T. Gruene, “3D-structured supports create complete data sets for electron crystallography,” *Nat. Commun.* **10** (2019) 3316.
- [64] S. W. Wilkins, T. E. Gureyev, D. Gao, A. Pogany & A. W. Stevenson, “Phase-contrast imaging using polychromatic hard X-rays,” *Nature* **384** (1996), 335-338.
- [65] R. M. Young, *An Introduction to Nonharmonic Fourier Series*. New York: Academic, 1980.
- [66] A. Zarrine-Afsar, T. R. M. Barends, C. Müller, M. R. Fuchs, L. Lomb, I. Schlichting and R. J. D. Miller, “Crystallography on a chip,” *Acta Cryst. D* **68** (2012), 321-323.

APPENDIX A. PROOF OF THEOREM 6.1

Since both diffraction patterns are from the same snapshot, we reset the object frame to have $\mathbf{l}_t = 0$.

Suppose the first alternative in (35) holds with $\mathbf{m}_t \neq 0$. By (41), $e^{i\kappa f_t}$ and $e^{i\kappa g_t}$ have the same autocorrelation function and hence

$$\sum_{\mathbf{n}} e^{i\kappa(f_t(\mathbf{n}+\mathbf{k}) - \overline{f_t(\mathbf{n})})} = \sum_{\mathbf{n}} e^{i\kappa(f_t(\mathbf{n}+\mathbf{m}_t+\mathbf{k}) - \overline{f_t(\mathbf{n}+\mathbf{m}_t)})} e^{i(\phi(\mathbf{n}+\mathbf{m}_t+\mathbf{k}) - \phi(\mathbf{n}+\mathbf{k}))} e^{-i(\phi(\mathbf{n}+\mathbf{m}_t) - \phi(\mathbf{n}))}$$

for all \mathbf{k} , or equivalently

$$(75) \quad \begin{aligned} & \sum_{\mathbf{n}} e^{i\kappa(f_{\mathbf{t}}(\mathbf{n}+\mathbf{m}_t+\mathbf{k})-\overline{f_{\mathbf{t}}(\mathbf{n}+\mathbf{m}_t)})} \\ &= \sum_{\mathbf{n}} e^{i\kappa(f_{\mathbf{t}}(\mathbf{n}+\mathbf{m}_t+\mathbf{k})-\overline{f_{\mathbf{t}}(\mathbf{n}+\mathbf{m}_t)})} e^{i(\phi(\mathbf{n}+\mathbf{m}_t+\mathbf{k})-\phi(\mathbf{n}+\mathbf{m}_t)-\phi(\mathbf{n}+\mathbf{k})+\phi(\mathbf{n}))} \end{aligned}$$

by change of index, $\mathbf{n} \rightarrow \mathbf{n} + \mathbf{m}_t$, on the left hand side of equation. Define

$$\Delta_{\mathbf{k}} f_{\mathbf{t}}(\mathbf{n} + \mathbf{m}_t) := f_{\mathbf{t}}(\mathbf{n} + \mathbf{m}_t + \mathbf{k}) - \overline{f_{\mathbf{t}}(\mathbf{n} + \mathbf{m}_t)}$$

and rewrite (75) as

$$(76) \quad 0 = \sum_n [e^{i(\phi(\mathbf{n}+\mathbf{m}_t+\mathbf{k})-\phi(\mathbf{n}+\mathbf{m}_t)-\phi(\mathbf{n}+\mathbf{k})+\phi(\mathbf{n}))} - 1] e^{i\kappa\Delta_{\mathbf{k}} f_{\mathbf{t}}(\mathbf{n}+\mathbf{m}_t)},$$

for all \mathbf{k} . We want to show that the probability of the event (76) is zero. Indeed, the right hand side of (76) almost surely does not vanish for any \mathbf{k} as follows.

Let us consider those summands in (76), for any fixed \mathbf{k} , that share a common $\phi(\mathbf{l})$, for any fixed \mathbf{l} , in the expression. Clearly, there are at most four such terms:

$$(77) \quad \begin{aligned} & [e^{i(\phi(\mathbf{l})-\phi(\mathbf{l}-\mathbf{k})-\phi(\mathbf{l}-\mathbf{m}_t)+\phi(\mathbf{l}-\mathbf{k}-\mathbf{m}_t))} - 1] e^{i\kappa\Delta_{\mathbf{k}} f_{\mathbf{t}}(\mathbf{l}-\mathbf{k})} \\ &+ [e^{i(\phi(\mathbf{l}+\mathbf{k})-\phi(\mathbf{l})-\phi(\mathbf{l}+\mathbf{k}-\mathbf{m}_t)+\phi(\mathbf{l}-\mathbf{m}_t))} - 1] e^{i\kappa\Delta_{\mathbf{k}} f_{\mathbf{t}}(\mathbf{l})} \\ &+ [e^{i(\phi(\mathbf{l}+\mathbf{m}_t)-\phi(\mathbf{l}-\mathbf{k}+\mathbf{m}_t)-\phi(\mathbf{l})+\phi(\mathbf{l}-\mathbf{k}))} - 1] e^{i\kappa\Delta_{\mathbf{k}} f_{\mathbf{t}}(\mathbf{l}-\mathbf{k}+\mathbf{m}_t)} \\ &+ [e^{i(\phi(\mathbf{l}+\mathbf{k}+\mathbf{m}_t)-\phi(\mathbf{l}+\mathbf{m}_t)-\phi(\mathbf{l}+\mathbf{k})+\phi(\mathbf{l}))} - 1] e^{i\kappa\Delta_{\mathbf{k}} f_{\mathbf{t}}(\mathbf{l}+\mathbf{m}_t)}. \end{aligned}$$

Since the continuous random variable $\phi(\mathbf{l})$ does not appear in other summands and hence is independent of them, (76) implies that (77) (and the rest of (76)) must vanish almost surely.

For \mathbf{k} that are linearly independent of \mathbf{m}_t , the four independent random variables

$$(78) \quad \phi(\mathbf{l} - \mathbf{k} - \mathbf{m}_t), \quad \phi(\mathbf{l} + \mathbf{k} - \mathbf{m}_t), \quad \phi(\mathbf{l} - \mathbf{k} + \mathbf{m}_t), \quad \phi(\mathbf{l} + \mathbf{k} + \mathbf{m}_t)$$

appear separately in exactly one summand in (77). Consequently, (77) (and hence (76)) almost surely does not vanishes for \mathbf{k} that are linearly independent of \mathbf{m}_t .

On the other hand, if \mathbf{k} is parallel to $\mathbf{m}_t \neq 0$, then for any

$$\mathbf{k} \notin \{\pm\mathbf{m}_{t_0}, \pm\frac{1}{2}\mathbf{m}_{t_0}, \pm 2\mathbf{m}_{t_0}\}$$

the four terms in (78) appear separately in exactly one summand in (77). Consequently, (77) almost surely does not vanishes.

Thus whenever the first alternative in (35) holds true $\mathbf{m}_t = 0$ and $e^{i\kappa g_{\mathbf{t}}} = e^{i\theta_{\mathbf{t}}} e^{i\kappa f_{\mathbf{t}}}$ for some constant $\theta_{\mathbf{t}}$ independent of the grid point.

Next, we show that the second alternative in (33) is false. By (41), we have

$$\sum_{\mathbf{n}} e^{i\kappa(f_{\mathbf{t}}(\mathbf{n}+\mathbf{k})-\overline{f_{\mathbf{t}}(\mathbf{n})})} = \sum_{\mathbf{n}} e^{-i\kappa(\overline{f_{\mathbf{t}}(-\mathbf{n}+\mathbf{m}_t+\mathbf{k})-f_{\mathbf{t}}(-\mathbf{n}+\mathbf{m}_t))}} e^{-i(\phi(-\mathbf{n}+\mathbf{m}_t+\mathbf{k})+\phi(\mathbf{n}+\mathbf{k}))} e^{i(\phi(-\mathbf{n}+\mathbf{m}_t)+\phi(\mathbf{n}))}$$

for all \mathbf{k} , or equivalently

$$(79) \quad \begin{aligned} & \sum_{\mathbf{n}} e^{i\kappa(f_{\mathbf{t}}(\mathbf{n} + \mathbf{m}_t + \mathbf{k}) - \overline{f_{\mathbf{t}}(\mathbf{n} + \mathbf{m}_t)})} \\ &= \sum_{\mathbf{n}} e^{-i\kappa(\overline{f_{\mathbf{t}}(-\mathbf{n} + \mathbf{m}_t + \mathbf{k})} - f_{\mathbf{t}}(-\mathbf{n} + \mathbf{m}_t))} e^{-i(\phi(-\mathbf{n} + \mathbf{m}_t + \mathbf{k}) + \phi(\mathbf{n} + \mathbf{k}))} e^{i(\phi(-\mathbf{n} + \mathbf{m}_t) + \phi(\mathbf{n}))} \end{aligned}$$

by change of index, $\mathbf{n} \rightarrow -\mathbf{n} + \mathbf{m}_t$, on the left hand side of equation. With

$$\Delta_{\mathbf{k}} \overline{f_{\mathbf{t}}(-\mathbf{n} + \mathbf{m}_t)} := \overline{f_{\mathbf{t}}(-\mathbf{n} + \mathbf{m}_t + \mathbf{k})} - f_{\mathbf{t}}(-\mathbf{n} + \mathbf{m}_t)$$

we rewrite (79) as

$$(80) \quad 0 = \sum_n [e^{i(-\phi(-\mathbf{n} + \mathbf{m}_t + \mathbf{k}) + \phi(-\mathbf{n} + \mathbf{m}_t) - \phi(\mathbf{n} + \mathbf{k}) + \phi(\mathbf{n}))} - 1] e^{-i\kappa \Delta_{\mathbf{k}} \overline{f_{\mathbf{t}}(-\mathbf{n} + \mathbf{m}_t)}}$$

for all \mathbf{k} . We want to show that the right hand side of (80) almost surely does not vanish for any \mathbf{k} .

As before, consider those summands in (80), for any fixed \mathbf{k} , that share a common $\phi(\mathbf{l})$, for any fixed \mathbf{l} , in the expression. Clearly, there are at most four such terms:

$$(81) \quad \begin{aligned} & [e^{i(-\phi(\mathbf{l}) + \phi(\mathbf{l} + \mathbf{k}) - \phi(-\mathbf{l} + \mathbf{m}_t) + \phi(-\mathbf{l} - \mathbf{k} + \mathbf{m}_t))} - 1] e^{-i\kappa \Delta_{\mathbf{k}} \overline{f_{\mathbf{t}}(\mathbf{l})}} \\ &+ [e^{i(-\phi(\mathbf{l} - \mathbf{k}) + \phi(\mathbf{l}) - \phi(-\mathbf{l} + \mathbf{k} + \mathbf{m}_t) + \phi(-\mathbf{l} + \mathbf{m}_t))} - 1] e^{-i\kappa \Delta_{\mathbf{k}} \overline{f_{\mathbf{t}}(\mathbf{l} - \mathbf{k})}} \\ &+ [e^{i(-\phi(-\mathbf{l} + \mathbf{m}_t) + \phi(-\mathbf{l} + \mathbf{k} + \mathbf{m}_t) - \phi(\mathbf{l}) + \phi(\mathbf{l} - \mathbf{k}))} - 1] e^{-i\kappa \Delta_{\mathbf{k}} \overline{f_{\mathbf{t}}(-\mathbf{l} + \mathbf{m}_t)}} \\ &+ [e^{i(-\phi(-\mathbf{l} - \mathbf{k} + \mathbf{m}_t) + \phi(-\mathbf{l} + \mathbf{m}_t) - \phi(\mathbf{l} + \mathbf{k}) + \phi(\mathbf{l}))} - 1] e^{-i\kappa \Delta_{\mathbf{k}} \overline{f_{\mathbf{t}}(-\mathbf{l} - \mathbf{k} + \mathbf{m}_t)}} \end{aligned}$$

With $\phi(\mathbf{l})$ appearing in no other terms, (80) implies that (81) must vanish almost surely.

Some observations are in order. First, both $\phi(\mathbf{l})$ and $\phi(-\mathbf{l} + \mathbf{m}_t)$ appear exactly once in each summand in (93). Second, the following pairings of the other phases

$$\{\phi(\mathbf{l} + \mathbf{k}), \phi(-\mathbf{l} - \mathbf{k} + \mathbf{m}_t)\}, \quad \{\phi(\mathbf{l} - \mathbf{k}), \phi(-\mathbf{l} + \mathbf{k} + \mathbf{m}_t)\}$$

also appear exactly twice in (93). As long as $\mathbf{k} \neq 0$ and $2\mathbf{l} \neq \mathbf{m}_t$, these two pairs are not identical and hence

$$(82) \quad \begin{aligned} 0 &= [e^{i(-\phi(\mathbf{l}) + \phi(\mathbf{l} + \mathbf{k}) - \phi(-\mathbf{l} + \mathbf{m}_t) + \phi(-\mathbf{l} - \mathbf{k} + \mathbf{m}_t))} - 1] e^{-i\kappa \Delta_{\mathbf{k}} \overline{f_{\mathbf{t}}(\mathbf{l})}} \\ &+ [\overline{[e^{i(\phi(-\mathbf{l} - \mathbf{k} + \mathbf{m}_t) - \phi(-\mathbf{l} + \mathbf{m}_t) + \phi(\mathbf{l} + \mathbf{k}) - \phi(\mathbf{l}))} - 1]} e^{-i\kappa \Delta_{\mathbf{k}} \overline{f_{\mathbf{t}}(-\mathbf{l} - \mathbf{k} + \mathbf{m}_t)}} \\ 0 &= [e^{i(-\phi(\mathbf{l} - \mathbf{k}) + \phi(\mathbf{l}) - \phi(-\mathbf{l} + \mathbf{k} + \mathbf{m}_t) + \phi(-\mathbf{l} + \mathbf{m}_t))} - 1] e^{-i\kappa \Delta_{\mathbf{k}} \overline{f_{\mathbf{t}}(\mathbf{l} - \mathbf{k})}} \\ &+ [\overline{[e^{i(\phi(-\mathbf{l} + \mathbf{m}_t) - \phi(-\mathbf{l} + \mathbf{k} + \mathbf{m}_t) + \phi(\mathbf{l}) - \phi(\mathbf{l} - \mathbf{k}))} - 1]} e^{-i\kappa \Delta_{\mathbf{k}} \overline{f_{\mathbf{t}}(-\mathbf{l} + \mathbf{m}_t)}} \end{aligned}$$

both of which are almost surely false because the two factors

$$[e^{i(-\phi(\mathbf{l}) + \phi(\mathbf{l} + \mathbf{k}) - \phi(-\mathbf{l} + \mathbf{m}_t) + \phi(-\mathbf{l} - \mathbf{k} + \mathbf{m}_t))} - 1], \quad [e^{i(-\phi(\mathbf{l} - \mathbf{k}) + \phi(\mathbf{l}) - \phi(-\mathbf{l} + \mathbf{k} + \mathbf{m}_t) + \phi(-\mathbf{l} + \mathbf{m}_t))} - 1]$$

differ with their complex conjugates in a random manner independently from $f_{\mathbf{t}}$.

Therefore, the second alternative in (35) almost surely does not hold true.

In summary, the first alternative in (35) holds with $\mathbf{m}_t = 0$, namely

$$\kappa g_{\mathbf{t}}(\mathbf{n}) = \theta_{\mathbf{t}} + \kappa f_{\mathbf{t}}(\mathbf{n}) \quad \text{mod } 2\pi$$

almost surely. Now that $g_{\mathbf{t}}(\mathbf{n}) = f_{\mathbf{t}}(\mathbf{n}) = 0$ for $\mathbf{n} \in \mathbb{Z}_p^2 \setminus \mathbb{Z}_{\ell_\alpha} \times \mathbb{Z}_{\ell_\beta}$ for $\mathbf{t} = (1, \alpha, \beta)$ due to the support constraint (21)-(22), so $\theta_{\mathbf{t}}$ must be an integer multiple of 2π .

The argument is complete.

APPENDIX B. PROOF OF THEOREM 6.3

Let

$$\begin{aligned} f_{\mathbf{t}_0}^*(\mathbf{n}) &= f_{\mathbf{t}_0}(\mathbf{n} + \mathbf{l}_{\mathbf{t}_0}), & f_{\mathbf{t}}^*(\mathbf{n}) &= f_{\mathbf{t}}(\mathbf{n} + \mathbf{l}_{\mathbf{t}}) \\ g_{\mathbf{t}_0}^*(\mathbf{n}) &= g_{\mathbf{t}_0}(\mathbf{n} + \mathbf{l}_{\mathbf{t}_0}), & g_{\mathbf{t}}^*(\mathbf{n}) &= g_{\mathbf{t}}(\mathbf{n} + \mathbf{l}_{\mathbf{t}}) \end{aligned}$$

for some $\mathbf{l}_{\mathbf{t}_0}, \mathbf{l}_{\mathbf{t}}$. The invariance property (37) of the uncoded diffraction patterns are independent of $\mathbf{l}_{\mathbf{t}_0}$:

$$(83) \quad |\mathcal{F}(e^{i\kappa f_{\mathbf{t}_0}})|^2 = |\mathcal{F}(e^{i\kappa f_{\mathbf{t}_0}^*})|^2, \quad |\mathcal{F}(e^{i\kappa g_{\mathbf{t}_0}})|^2 = |\mathcal{F}(e^{i\kappa g_{\mathbf{t}_0}^*})|^2$$

and hence we may assume $\mathbf{l}_{\mathbf{t}_0} = \mathbf{l}_{\mathbf{t}} = 0$ by resetting the object frame.

The structure of the argument is entirely analogous to the proof of Theorem 6.1 with the exceptions that \mathbf{k} is now limited to $P_{\mathbf{t}_0} \cap P_{\mathbf{t}}$ as a result of applying Fourier slice theorem.

To adapt the argument with one Fourier slice to the setting of two Fourier slices we slightly abuse the notation and treat the boldfaced vectors in Appendix A as embedded in the 3D Fourier space here.

APPENDIX C. PROOF OF THEOREM 7.1

The proof of Theorem 7.1 is analogous to that of Theorem 6.1, except with the additional complication of possible vanishing of the object function under the Born approximation.

Similar to Proposition 4.1, for the diffraction pattern given by (47) we have the following characterization.

Proposition C.1. [17] *Let μ be the phase mask with phase continuously and independently distributed. Suppose that $\text{supp}(f_{\mathbf{t}})$ is not a subset of a line and another masked object projection $g_{\mathbf{t}}^* := \nu g_{\mathbf{t}}$ produces the same diffraction pattern as $f_{\mathbf{t}}^* = \mu \odot f_{\mathbf{t}}$. Then for some \mathbf{p} and θ*

$$(84) \quad f_{\mathbf{t}}^*(\mathbf{n} + \mathbf{p}) = e^{-i\theta} g_{\mathbf{t}}^*(\mathbf{n}) \quad \text{or} \quad e^{i\theta} \text{Twin}(g_{\mathbf{t}}^*)(\mathbf{n})$$

for all \mathbf{n} .

If μ is completely known, then $\nu = \mu$ and (84) becomes

$$(85) \quad g_{\mathbf{t}}(\mathbf{n})\mu(\mathbf{n}) = \begin{cases} e^{i\theta_{\mathbf{t}}} f_{\mathbf{t}}(\mathbf{n} + \mathbf{m}_{\mathbf{t}})\mu(\mathbf{n} + \mathbf{m}_{\mathbf{t}}) \\ e^{i\theta_{\mathbf{t}}} f_{\mathbf{t}}(-\mathbf{n} + \mathbf{m}_{\mathbf{t}})\mu(-\mathbf{n} + \mathbf{m}_{\mathbf{t}}). \end{cases}$$

First suppose that the first alternative in (85) and we want to show that $\mathbf{m}_{\mathbf{t}} = 0$, which then implies that $g_{\mathbf{t}}(\cdot) = e^{i\theta_{\mathbf{t}}} f_{\mathbf{t}}(\cdot)$.

Equality of the uncoded diffraction (50) implies that the autocorrelation of g_t equals that of f_t and hence by (85)

$$\sum_{\mathbf{n} \in \mathbb{Z}_p^2} f_t(\mathbf{n} + \mathbf{k}) \overline{f_t(\mathbf{n})} = \sum_{\mathbf{n} \in \mathbb{Z}_p^2} f_t(\mathbf{n} + \mathbf{k} + \mathbf{m}_t) \overline{f_t(\mathbf{n} + \mathbf{m}_t)} \mu(\mathbf{n} + \mathbf{k} + \mathbf{m}_t) \mu(\mathbf{n}) \overline{\mu(\mathbf{n} + \mathbf{k}) \mu(\mathbf{n} + \mathbf{m}_t)}$$

which, after change of index $\mathbf{n} \rightarrow \mathbf{n} + \mathbf{m}_t$ on the left hand side, becomes

$$(86) \quad 0 = \sum_{\mathbf{n} \in \mathbb{Z}_p^2} f_t(\mathbf{n} + \mathbf{k} + \mathbf{m}_t) \overline{f_t(\mathbf{n} + \mathbf{m}_t)} [e^{i(\phi(\mathbf{n} + \mathbf{k} + \mathbf{m}_t) - \phi(\mathbf{n} + \mathbf{m}_t) + \phi(\mathbf{n}) - \phi(\mathbf{n} + \mathbf{k}))} - 1]$$

for all $\mathbf{k} \in \mathbb{Z}_{2p-1}^2$. It is convenient to consider the autocorrelation function as $(2p-1)$ -periodic function and endow \mathbb{Z}_{2p-1}^2 with the periodic boundary condition.

Let us consider those summands on the right side of (86), for any fixed \mathbf{k} , that share a common $\phi(\mathbf{l})$, for any fixed \mathbf{l} . Clearly, there are at most four such terms:

$$(87) \quad \begin{aligned} & [e^{i(\phi(\mathbf{l}) - \phi(\mathbf{l} - \mathbf{k}) - \phi(\mathbf{l} - \mathbf{m}_t) + \phi(\mathbf{l} - \mathbf{k} - \mathbf{m}_t))} - 1] f_t(\mathbf{l}) \overline{f_t(\mathbf{l} - \mathbf{k})} \\ & + [e^{i(\phi(\mathbf{l} + \mathbf{k}) - \phi(\mathbf{l}) - \phi(\mathbf{l} + \mathbf{k} - \mathbf{m}_t) + \phi(\mathbf{l} - \mathbf{m}_t))} - 1] f_t(\mathbf{l} + \mathbf{k}) \overline{f_t(\mathbf{l})} \\ & + [e^{i(\phi(\mathbf{l} + \mathbf{m}_t) - \phi(\mathbf{l} - \mathbf{k} + \mathbf{m}_t) - \phi(\mathbf{l}) + \phi(\mathbf{l} - \mathbf{k}))} - 1] f_t(\mathbf{l} + \mathbf{m}_t) \overline{f_t(\mathbf{l} - \mathbf{k} + \mathbf{m}_t)} \\ & + [e^{i(\phi(\mathbf{l} + \mathbf{k} + \mathbf{m}_t) - \phi(\mathbf{l} + \mathbf{m}_t) - \phi(\mathbf{l} + \mathbf{k}) + \phi(\mathbf{l}))} - 1] f_t(\mathbf{l} + \mathbf{k} + \mathbf{m}_t) \overline{f_t(\mathbf{l} + \mathbf{m}_t)}. \end{aligned}$$

Since the continuous random variable $\phi(\mathbf{l})$ does not appear in other summands and hence is independent of them, (86) implies that (87) (and the rest of (86)) vanishes almost surely.

Suppose $\mathbf{m}_t \neq 0$ and consider any \mathbf{k} that is linearly independent of \mathbf{m}_t . The four independent random variables

$$(88) \quad \phi(\mathbf{l} - \mathbf{k} - \mathbf{m}_t), \quad \phi(\mathbf{l} + \mathbf{k} - \mathbf{m}_t), \quad \phi(\mathbf{l} - \mathbf{k} + \mathbf{m}_t), \quad \phi(\mathbf{l} + \mathbf{k} + \mathbf{m}_t)$$

appear separately in exactly one summand in (87). Consequently, (87) can not vanish, unless

$$(89) \quad f_t(\mathbf{l}) \overline{f_t(\mathbf{l} - \mathbf{k})} = 0, \quad \overline{f_t(\mathbf{l})} f_t(\mathbf{l} + \mathbf{k}) = 0$$

$$(90) \quad f_t(\mathbf{l} + \mathbf{m}_t) \overline{f_t(\mathbf{l} - \mathbf{k} + \mathbf{m}_t)} = 0, \quad \overline{f_t(\mathbf{l} + \mathbf{m}_t)} f_t(\mathbf{l} + \mathbf{k} + \mathbf{m}_t) = 0$$

in (87).

On the other hand, if \mathbf{k} is parallel to $\mathbf{m}_t \neq 0$, then for any

$$(91) \quad \mathbf{k} \notin \{\pm \mathbf{m}_{t_0}, \pm \frac{1}{2} \mathbf{m}_{t_0}, \pm 2 \mathbf{m}_{t_0}\}$$

the four terms in (88) appear separately in exactly one summand in (87). Consequently, (87) (and hence (86)) almost surely does not vanish unless (89) and (90) hold.

Consider $\mathbf{k} = 0$ which satisfies (91) if $\mathbf{m}_t \neq 0$. Clearly (89)-(90) with $\mathbf{k} = 0$ implies that $f_t \equiv 0$, which violate the assumption that $\text{supp}(f_t)$ is not a subset of a line. Thus $\mathbf{m}_t = 0$ in the first alternative in (85).

Next we prove that the second alternative in (85) is false for all \mathbf{m}_t . Otherwise, by (50) we have

$$\begin{aligned} & \sum_{\mathbf{n} \in \mathbb{Z}_p^2} f_t(\mathbf{n} + \mathbf{k}) \overline{f_t(\mathbf{n})} \\ &= \sum_{\mathbf{n} \in \mathbb{Z}_p^2} \overline{f_t(-\mathbf{n} - \mathbf{k} + \mathbf{m}_t)} f_t(-\mathbf{n} + \mathbf{m}_t) \overline{\mu(-\mathbf{n} - \mathbf{k} + \mathbf{m}_t) \mu(\mathbf{n} + \mathbf{k})} \mu(\mathbf{n}) \mu(-\mathbf{n} + \mathbf{m}_t) \end{aligned}$$

which, after change of index $\mathbf{n} \rightarrow -\mathbf{n} - \mathbf{k} + \mathbf{m}_t$ on the left hand side, becomes

$$(92)0 = \sum_{\mathbf{n} \in \mathbb{Z}_p^2} \overline{f_t(-\mathbf{n} - \mathbf{k} + \mathbf{m}_t)} f_t(-\mathbf{n} + \mathbf{m}_t) [e^{i(-\phi(-\mathbf{n} - \mathbf{k} + \mathbf{m}_t) + \phi(-\mathbf{n} + \mathbf{m}_t) - \phi(\mathbf{n} + \mathbf{k}) + \phi(\mathbf{n}))} - 1]$$

for all $\mathbf{k} \in \mathbb{Z}_{2p-1}^2$.

Consider those summands in (92), for any fixed \mathbf{k} , that share a common $\phi(\mathbf{l})$, for any fixed \mathbf{l} . Clearly, there are at most four such terms:

$$(93) \quad \begin{aligned} & [e^{i(-\phi(\mathbf{l}) + \phi(\mathbf{l} + \mathbf{k}) - \phi(-\mathbf{l} + \mathbf{m}_t) + \phi(-\mathbf{l} - \mathbf{k} + \mathbf{m}_t))} - 1] \overline{f_t(\mathbf{l})} f_t(\mathbf{l} + \mathbf{k}) \\ & + [e^{i(-\phi(\mathbf{l} - \mathbf{k}) + \phi(\mathbf{l}) - \phi(-\mathbf{l} + \mathbf{k} + \mathbf{m}_t) + \phi(-\mathbf{l} + \mathbf{m}_t))} - 1] \overline{f_t(\mathbf{l} - \mathbf{k})} f_t(\mathbf{l}) \\ & + [e^{i(-\phi(-\mathbf{l} + \mathbf{m}_t) + \phi(-\mathbf{l} + \mathbf{k} + \mathbf{m}_t) - \phi(\mathbf{l}) + \phi(\mathbf{l} - \mathbf{k}))} - 1] \overline{f_t(-\mathbf{l} + \mathbf{m}_t)} f_t(-\mathbf{l} + \mathbf{k} + \mathbf{m}_t) \\ & + [e^{i(-\phi(-\mathbf{l} - \mathbf{k} + \mathbf{m}_t) + \phi(-\mathbf{l} + \mathbf{m}_t) - \phi(\mathbf{l} + \mathbf{k}) + \phi(\mathbf{l}))} - 1] \overline{f_t(-\mathbf{l} - \mathbf{k} + \mathbf{m}_t)} f_t(-\mathbf{l} + \mathbf{m}_t) \end{aligned}$$

which must vanish under (92).

Some observations are in order. First, both $\phi(\mathbf{l})$ and $\phi(-\mathbf{l} + \mathbf{m}_t)$ appear exactly once in each summand in (93). Second, the following pairings of the other phases

$$(94) \quad \{\phi(\mathbf{l} + \mathbf{k}), \phi(-\mathbf{l} - \mathbf{k} + \mathbf{m}_t)\}, \quad \{\phi(\mathbf{l} - \mathbf{k}), \phi(-\mathbf{l} + \mathbf{k} + \mathbf{m}_t)\}$$

also appear exactly twice in (93). As long as

$$(95) \quad \begin{aligned} \mathbf{k} &\neq 0 \\ \& \mathbf{l} \neq \mathbf{m}_t/2, \end{aligned}$$

the two sets in (94) are not identical and, since each contains at least one element that is independent of the other, we have

$$(96) \quad 0 = [e^{i(-\phi(\mathbf{l}) + \phi(\mathbf{l} + \mathbf{k}) - \phi(-\mathbf{l} + \mathbf{m}_t) + \phi(-\mathbf{l} - \mathbf{k} + \mathbf{m}_t))} - 1] \overline{f_t(\mathbf{l})} f_t(\mathbf{l} + \mathbf{k}) \\ + [e^{i(\phi(-\mathbf{l} - \mathbf{k} + \mathbf{m}_t) - \phi(-\mathbf{l} + \mathbf{m}_t) + \phi(\mathbf{l} + \mathbf{k}) - \phi(\mathbf{l}))} - 1] \overline{f_t(-\mathbf{l} - \mathbf{k} + \mathbf{m}_t)} f_t(-\mathbf{l} + \mathbf{m}_t)$$

$$(97) \quad 0 = [e^{i(-\phi(\mathbf{l} - \mathbf{k}) + \phi(\mathbf{l}) - \phi(-\mathbf{l} + \mathbf{k} + \mathbf{m}_t) + \phi(-\mathbf{l} + \mathbf{m}_t))} - 1] \overline{f_t(\mathbf{l} - \mathbf{k})} f_t(\mathbf{l}) \\ + [e^{i(\phi(-\mathbf{l} + \mathbf{m}_t) - \phi(-\mathbf{l} + \mathbf{k} + \mathbf{m}_t) + \phi(\mathbf{l}) - \phi(\mathbf{l} - \mathbf{k}))} - 1] \overline{f_t(-\mathbf{l} + \mathbf{m}_t)} f_t(-\mathbf{l} + \mathbf{k} + \mathbf{m}_t).$$

Because the two factors

$$[e^{i(-\phi(\mathbf{l}) + \phi(\mathbf{l} + \mathbf{k}) - \phi(-\mathbf{l} + \mathbf{m}_t) + \phi(-\mathbf{l} - \mathbf{k} + \mathbf{m}_t))} - 1], \quad [e^{i(-\phi(\mathbf{l} - \mathbf{k}) + \phi(\mathbf{l}) - \phi(-\mathbf{l} + \mathbf{k} + \mathbf{m}_t) + \phi(-\mathbf{l} + \mathbf{m}_t))} - 1]$$

differ with their complex conjugates in a random manner independently from f_t , both (96) and (97) are almost surely false unless

$$(98) \quad \overline{f_t(\mathbf{l})} f_t(\mathbf{l} + \mathbf{k}) = 0, \quad f_t(\mathbf{l}) \overline{f_t(\mathbf{l} - \mathbf{k})} = 0,$$

$$(99) \quad f_t(-\mathbf{l} + \mathbf{m}_t) \overline{f_t(-\mathbf{l} - \mathbf{k} + \mathbf{m}_t)} = 0, \quad \overline{f_t(-\mathbf{l} + \mathbf{m}_t)} f_t(-\mathbf{l} + \mathbf{k} + \mathbf{m}_t) = 0.$$

On the other hand, if $\mathbf{l} = \mathbf{m}_t/2$ but $\mathbf{k} \neq 0$, then

$$(100) \quad \mathbf{l} + \mathbf{k} = -\mathbf{l} + \mathbf{k} + \mathbf{m}_t \neq -\mathbf{l} - \mathbf{k} + \mathbf{m}_t = \mathbf{l} - \mathbf{k},$$

and hence (93) = 0 becomes

$$0 = [e^{i(-2\phi(\mathbf{l})+\phi(\mathbf{l}+\mathbf{k})+\phi(\mathbf{l}-\mathbf{k}))} - 1] \overline{f_t(\mathbf{l})} f_t(\mathbf{l} + \mathbf{k}) + [\overline{e^{i(-2\phi(\mathbf{l})+\phi(\mathbf{l}+\mathbf{k})+\phi(\mathbf{l}-\mathbf{k}))} - 1}] \overline{f_t(\mathbf{l}-\mathbf{k})} f_t(\mathbf{l})$$

implying (98). In other words, (98) holds true for $\mathbf{k} \neq 0$.

Now we show that (98) for $\mathbf{k} \neq 0$ implies that f_t has at most one nonzero pixel.

Suppose that $f_t(\mathbf{l}) \neq 0$ for some \mathbf{l} . Then by (98), $f_t(\mathbf{n}) = 0$ for all other $\mathbf{n} \neq \mathbf{l}$, i.e. f_t is a singleton which contradicts the assumption that $\text{supp}(f_t)$ is not a subset of a line.

Consequently the second alternative in (85) is false almost surely. The proof is now complete.

APPENDIX D. PROOF OF THEOREM 7.3

The invariance property (29) of the uncoded diffraction patterns are independent of \mathbf{l}_{t_0} :

$$(101) \quad |\mathcal{F}(f_{t_0})|^2 = |\mathcal{F}(f_{t_0}^*)|^2, \quad |\mathcal{F}(g_{t_0})|^2 = |\mathcal{F}(g_{t_0}^*)|^2$$

and hence we may assume $\mathbf{l}_{t_0} = \mathbf{l}_t = 0$ by resetting the object frame.

The structure of the argument is entirely analogous to the proof of Theorem 7.1 with the exceptions that \mathbf{k} is now limited to $P_{t_0} \cap P_t$ as a result of applying Fourier slice theorem.

To adapt the argument with one Fourier slice to the setting of two Fourier slices we slightly abuse the notation and treat the boldfaced vectors in Appendix C as embedded in the 3D Fourier space here.

DEPARTMENT OF MATHEMATICS, UNIVERSITY OF CALIFORNIA, DAVIS, CALIFORNIA 95616, USA. EMAIL: FANNJIANG@MATH.UCDAVIS.EDU